Università di Pisa
Dipartimento di Fisica

Tesi di Laurea Magistrale

Anno Accademico 2014/2015

Building of tri-axial strain gauge based on FBG sensors

Candidate:
Umberto Giacomelli

Advisors:
Prof. Niccolò Beverini
Dott. Enrico Maccioni

Contents

CHAPTER 1

Introduction

1.1 The importance of geohazard study

The San Andreas Fault, the entire Japan island and Italy are just some examples of the active seismic and volcanic zones around the world. The community of people living in these

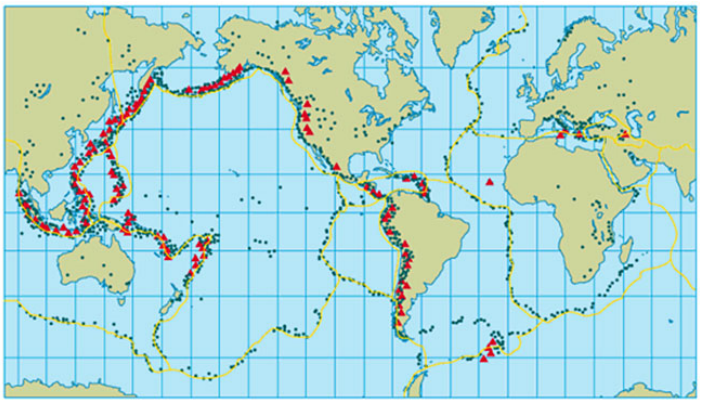

Figure 1.1: Image from Pregliasco website [1]. Maps of world seismic (•) and volcanic (▲) zones. The yellow line are the edge of tectonic plates

places had to learn how to survive to these phenomena. In recent and past history there are anyway many examples of catastrophes (e.g. L'Aquila 2006, Sendai and Tohoku 2011). Science and technology have the task of seeking always best way to avoid damage and casualties, and to teach people how to face that kind of events. A glaring example of this is the comparison between two recent earthquakes: the one with a magnitude 6.3 on 14 march 2014 in the Kyushu (Japan) and the one with a magnitude 5.8 on 6 April 2009 in the L'Aquila (Italy). In the first case thanks to the last technology achievements, especially in buildings construction, the earthquake caused only about twenty injuries. In the second one, even if the magnitude is lower, the earthquake caused 309 dead and 1600 injuries. From the ruins it was clear that the techniques used to build the buildings was inappropriate to a seismic zone like that.

"I terremoti non si possono prevedere, ma le conseguenze si" [2]

This sentence summarizes the final goal of studies about all kinds of seismic events. We can not predict where and when these events might occur, but we must be able to predict

their consequences and hence we must take the appropriate precautions. In order to improve the knowledge of seismic and volcanic activity, in 2007 during the third International Geohazards Workshop the Frascati Declaration was adopted. Some of the most important things of this declaration are: the choice to use both spatial and in-situ geophysical data, to correctly monitoring geohazards; the decision to contribute to the Hyogo Framework for Action (HFA), a 10-year plan of United Nations to make the world safer from natural hazards; to incentive an international effort in monitoring and studying the sites of particular geological interest, defined as **Supersite**. Four years later the European Union financed 3 projects **FUTUREVOLC**, **MARSite** and **MEDiterranean SUpersite Volcanoes (MED-SUV)** under the overarching coordination of **European Plate Observing System (EPOS)**. The FUTUREVOLC project concerns a long term monitoring experiment in geologically active regions of Europe prone to natural hazards. MARSite is a project with the aim of assessing the state of the art of seismic risk evaluation and management at European level. The MED-SUV deals is to improve the capacities of scientific institutions, end users and SMEs (Small and Medium Enterprises) that forming the project consortium to assess volcanic hazards at Italian supersites.

1.2 The MED-SUV Project

The European supersites are four split in three countries: Italy, Iceland and Turkey. MED-SUV works with the Italian ones, that are: **Etna** and **Campi Flegrei/Vesuvius**. The project is based on comparing data coming from different fields of analysis i.e. geophysics, volcanology, geochemic and Earth Observation (EO) data. In this way we are able to characterize the peculiar behaviours of volcano before and during the entire eruptive phase.
The volcanic hazard assessment will be improved thanks to the results got by MED-SUV. The cooperation with Small and Middle Enterprises (SMEs) and scientists, instead, will increase awareness and training on the risks related to the volcanic supersites. Moreover, this partnership will produce important impacts on the European industrial sector.
The project is split in eight working packages (Fig. 1.2):

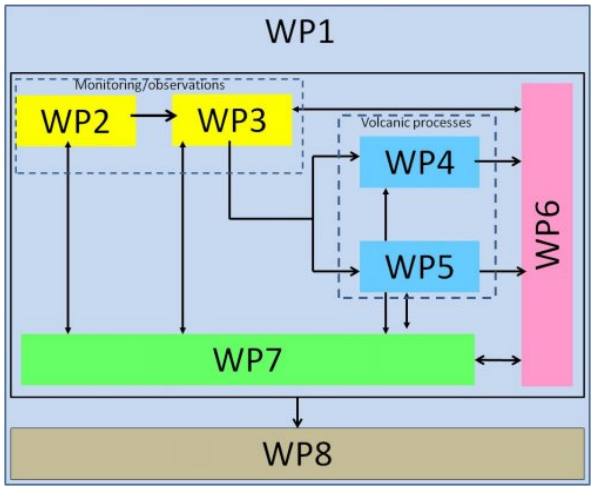

Figure 1.2: Med-Suv Working Packages

- WP1 : Project management
- WP2 : New Monitoring and Observing Systems
- WP3 : Data Sharing, Integration and Interoperability
- WP4 : Closed-conduit volcanoes laboratory
- WP5 : Etna volcano laboratory
- WP6 : Hazard assessment, disaster preparedness and mitigation
- WP7 : Pilot Phase
- WP8 : Dissemination and Outreach

1.2.1 WP2

This thesis project is a collaboration with **Marwan Technology**, a Spin off company of the Department of Physics of Pisa University, which is involved in WP2. The target of WP2 is to develop a new monitoring systems specifically projected to measurements in volcanic environment, increase measurements accuracy and precision with respect to previously ones [3], increment the spatial/temporal data sampling and reduce the costs of collection of the information. Moreover, due to the inaccessibility of the area in which this system will be installed from the final part of autumn to the mid spring, the system must be designed to work without direct human control or with a remote control. Thanks to the wide spectrum of volcanic phenomena on the cluster of Supersites we will have the opportunity to develop and test the systems in different operative conditions.
In its turn the WP2 is divided in two sub-tasks

- Remote Sensing
- In-Situ Task

The Remote Sensing is developed and operated by **Deutsches Zentrum fuer Luft - und Raumfahrt (DLR)**. They will implement two systems to use the Synthetic Aperture Radar (SAR) in the field of MED-SUV. The first one provides the use of X-band of radar in order to monitoring ground deformations over active volcanoes. The second one is to implement a methodology to explore the potential use of C-band of SAR in the characterization of volcanic plumes in terms of geophysical parameters.
The In-Situ Task is focusing on realizing a new low cost and high resolution sensor based on optical Fiber Bragg Grating (FBG) and a low power consuming and low priced dataloggers as data acquisition system. Moreover, this division of WP2 has also the assignment of realizing new instruments and sensors to measure the physical and chemical parameters of volcanic emissions (e.g. volcanic plumes and fumaroles) and to monitor the lava flow thermal and spatial evolution. This thesis is finalized to the realization of a tri-axial strain gauge based on FBGs and its interrogation system

1.3 Plastic and elastic behaviour of rock

FBGs are widely used in civil engineering field as strain gauge [4–8] and recently also in geology [9–11]. Thus far, in this field, FBGs have been used to measure rocks movements among faults [10]. This categories of measurements require one sensor tied to the rocks on the two sides of a fault. Our sensor function is different from this, it must be able to measure the deformations of a single rock along vertical and horizontals directions. To interpret the data coming from these measurements correctly, we need to know which kind of deformation we are studying. In physics the deformations are divided in two kinds: plastic or irreversible and elastic or reversible. All of solid materials can be deformed in both ways; in Fig. 1.4 are shown two examples of stress-strain curve. These ones discern the types of deformations depending on the stress and strain. Both (stress and strain) are a second order tensor; the first one (σ_{ij}) is defined as

$$\partial_j \sigma_{ij} = f_i \tag{1.1}$$

where f_i is the i-th component of applied force per unit volume; the second one (u_{ij}) is defined as

$$u_{ij} = \frac{1}{2}\left(\frac{\partial u_i}{\partial x_j} + \frac{\partial u_j}{\partial x_i} + \frac{\partial u_l}{\partial x_i}\frac{\partial u_l}{\partial x_j}\right) \tag{1.2}$$

where u_i are the displacements and x_i the length [12]. The diagonal elements of strain tensor are also called *normal strain* (normal strain are typically indicated with Greek letter ε: $\varepsilon_{ii} = u_{ii}$), they describe the relative length variation along the variation length direction (see Fig. 1.3). In Fig. 1.4 we use σ and ε because these kind of curve are evaluated in laboratory

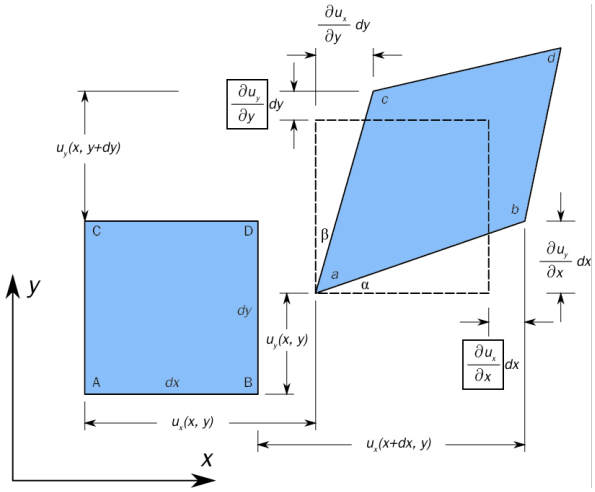

Figure 1.3: Example of a 2D deformation, the normal stress are the boxed fractions[1]

using the process of *simple traction (or compression)*. During this kind of process σ_{ij} has only one component different from 0, the one on the diagonal in correspondence to the direction of applied force on the tested sample; while, due to the relation between u_{ij} and σ_{ij} (Eq. 1.5), the strain tensor is diagonal. Therefore, in plots of stress-strain curve $\sigma = \sigma_{ii} \neq 0$ and ε is the element on the diagonal of u_{ij} in correspondence to the non zero one of σ_{ij}. E.g. if we stretch the sample along the z axis we get $\sigma = \sigma_{zz}$ and $\varepsilon = u_{zz}$. Stress-strain curves are the function that describe and classify the deformations for each materials. These curves behaviour are determined by the internal proprieties of the studied elements, e.g. density, hardness, temperature, etc. In our case the element at issue is basalt rock, which belongs to the brittle elements category, hence we focus on the curve in Fig. 1.4b. The elasticity limit of this kind of rock is of the order of 1 [GPa] and 0.01 [ε] [13]. Thanks to the previous measurements made by Bonaccorso *et al.* [3], we can estimate that the strain that we will have to measure is of the order of tens of micro-strain, hence for all of this work we will consider the rock deformations as elastic ones.

Assuming to work with isotropic material we can use the deformation description of the elasticity theory [12]. It describes the deformations trough the tensors of strain and stress and two[2] of the six constants: bulk modulus (K), Young's modulus (E), Lamé's first parameter (λ), Shear modulus (μ), Poisson's ratio (ν), P-wave modulus (M). We choose the Young's modulus (E) and the Poisson's ratio (ν). The first one is defined as the ratio between the

[1] Re-adapted from https://en.wikipedia.org/wiki/Infinitesimal_strain_theory#/media/File:2D_geometric_strain.svg

[2] these constants are related each other by four equation

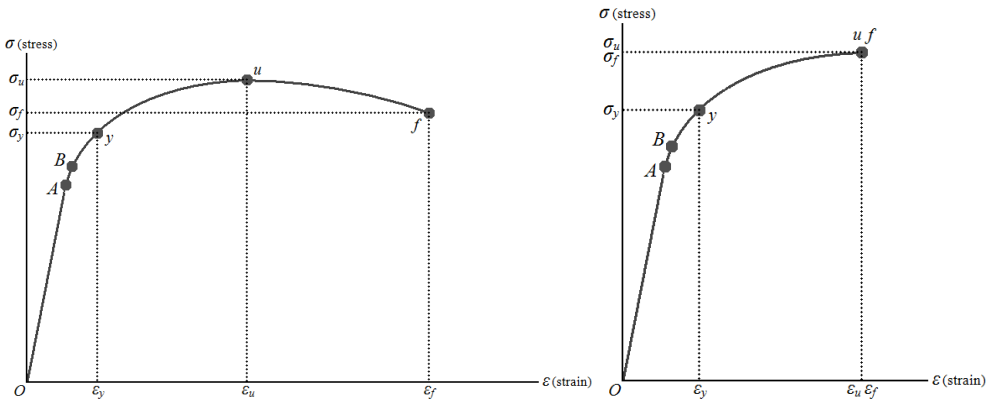

(a) Ductile material. (b) Brittle material.

Figure 1.4: Examples of stress-starin curves. A is the elastic limit and B the proportionality one. y is the yield point, starting from this point higher strains cause permanent deformation. u and f are the ultimate and the fracture strain, respectively. The first one is the maximum stress that a material can withstand without failing or breaking, the second one is the rupture point.

applied stress and consequent strain along the same axis[3].

$$E = \frac{\sigma_{ii}}{\varepsilon_{ii}} \tag{1.3}$$

The second one is defined as

$$\nu = -\frac{\varepsilon_T}{\varepsilon_L} \tag{1.4}$$

were ε_T is the normal strain along the axis transversal to the compression (or stretch) direction and ε_L is that along the longitudinal one. Except for auxetic materials, the signs of ε_T and ε_L are different. When a solid is compressed (elongated) in one direction, it usually tends to expand (compress) in the other two directions perpendicular to the compression (elongation) one, that is the so called *Poisson effect* (Fig. 1.5). Using these two constant we

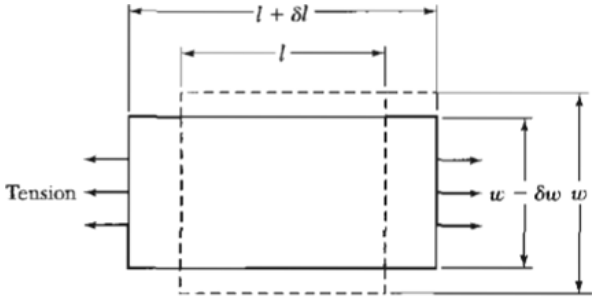

Figure 1.5: Example of the Poisson effect. Lateral traction generates a trasversal contraction

can write the relation between u_{ij} and σ_{ij}

$$\sigma_{ij} = \frac{E}{1+\nu}\left(u_{ij}\left(1-\nu\right) + \frac{\nu}{1-2\nu}u_{ll}\delta_{ij}\right) \tag{1.5}$$

From now on, unless otherwise specified, with strain we mean normal strain, and in order to simplify the notation we write ε_i instead of ε_{ii}.

[3] the slope of elastic zone of Fig. 1.4

CHAPTER 2

Fiber Bragg Gratings

2.1 Overview of optical fiber

In 1840 Daniel Collodon [14] and Jacques Babinet [15] showed that light could be guided along jets of water for fountain displays. This is the first example of wave guide built using refraction index; 48s years later for the first time, in medical field, a tube of bent glass has been used to illuminate body cavities. These works showed that a ray of light can be "bent" using reflections and refractions. In 1954 Abraham van Heel [16] showed how to simultaneously improve the internal reflection and reduce the noise caused by external light. He covered the glass tube used as light guide with a transparent cladding, getting a combination refraction index that made possible the total reflection. In this way the light inside the tube hardly came out before the end of it. This innovation increased the fibers performances thanks to an appropriate choice of materials. This choice is based on the materials refraction index in order to take advantage of the total reflection. Later a third layer as a protection to the fiber was added: the coating[1].

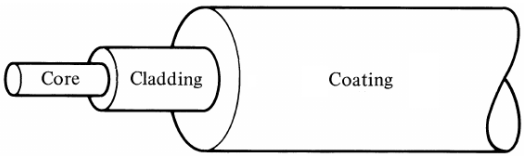

Figure 2.1: Scheme of an optical fiber

The turning point in the history of optical fiber comes on the first of April 1966 thanks to Charles K. Kao and George Hockham at the meeting of the Institution of Electrical Engineers in London. Until that day the main problem for optical fiber was the high signal loss. Kao and Hockham discovered that this problem was due to the impurity in the fiber and not to the fiber itself. So during the meeting they presented a paper in which they supported the idea of:

"Despite the fact that the best readily available low-loss material has a loss of about 1000 dB/km, STL[2] believes that materials having losses of only tens of decibels per kilometre will eventually be developed."

[1] Today some fibers have a coating built by several layers depending on fibers use
[2] Standard Telecommunications Laboratories

The presentation persuaded both academics and investors all over the world to start researches projects in order to reduce the fiber losses. Thanks to this idea Kao will win the Nobel Prize in 2009. Of all of research groups that working on fiber loss the most important was the one of Corning Glass Works, now Corning Incorporated, composed by Robert Maurer, Donald Keck and Peter Schultz. In 1970 through a process of doping they managed to increase the refractive index of the core slightly above that of the cladding, but without raising the attenuation dramatically. The fiber that they built was the first with a loss less than 20[dB/km][3]. Since this moment the optical fiber, thanks to their features, upset the word of telecommunications.

2.2 Fiber Bragg Gratings

Two are the mains advantages of working with fibers: the first, as already said, is the low signal attenuation. The second one is that they need only a source of light, at the input, and a photo sensitive receiver at the output, without any electrical connection. These aspects make fibers very good devices to communicate, but despite these qualities, fibers had a non negligible drawback: the difficult integration with the other optical components (lens, mirror, wavelength selector and so on). Combining an optical fiber with some of these components involves a huge insertion loss, and the advantages that we have using fiber could be lost in this kind of connections. Moreover, using fibers with external components exposes the whole system to sources of error like external light, imperfect alignment of optical components etc.
Some of these complications have been solved by using techniques suitable to alter the core index of refraction of optical fibers. With these techniques we are able to create a periodic pattern inside the fiber core that acts like a selective mirror for wavelengths that satisfy the Bragg condition. **Fiber Bragg Gratings** (**FIG**) [17] are Bragg gratings realized directly inside the core. Hill and his group [18] studied the index of refraction changes inside the fiber core. They discovered the **Photosensitivity**, that is the capability of light to induce permanent refractive index changes in the fiber core [19]

2.2.1 Photosensitivity

Hill and his team during their experiment used a germanium-doped silica optical fiber in which they launched visible light from an argon ion laser with a wavelength of 488 [nm]. The prolonged exposure of the fiber to the laser light gave rise to an increase in the attenuation of the fiber transmission. This effect is due to the laser light interference with the Fresnel reflected beam. The intensity of the interference peaks formed in this way has a spatial periodicity as long as the sources wavelength. After several tens of seconds, in correspondence to the interference peaks, the core refraction index start to change, at the end we have a perturbation of the refractive index with the same periodicity of the peaks. The presence of this refractive-index grating, called *self-organized* or *self-induced* gratings, produces an increase in the back reflection of the fiber to a value many times higher than that of the Fresnel reflection ($\sim$ 4% in this case). This increase is shown in Fig. 2.2 from Hill's paper [18]
At the beginning there was not too much interest in this research field since that photosensitivity was viewed as a phenomenon present only in this special fibers. About ten years later Hill's work, Stone [20] found photosensitivity in many different germanium doped fibers.

[3]Nowadays we are able to realize fiber first with a loss less than 0.3[dB/km]

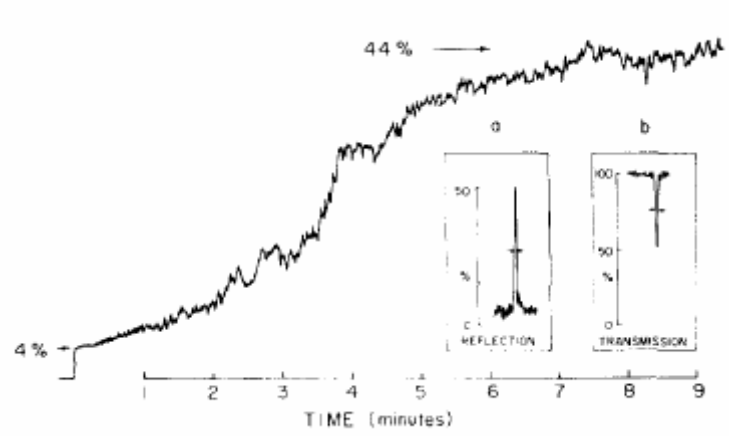

Figure 2.2: Figure number 2 and its caption of Hill's paper [18]. Build-up in time of the reflectivity of a 1 [m] strand of Ge-doped core optical fiber (NA $= 0.1$, core diameter $= 2.5\,[\mu\text{m}]$). The guide is carrying 1 [W] of single-mode 488.0 [nm] light; the filter structure is seeded by the fiber-output-end Fresnel back reflection. Note that the filter reflects the light in the core; therefore, assuming a realistic launch efficiency $= 50\%$, the true reflectivity of this filter is correspondingly 88%. Insets (a) and (b) show respectively typical reflection and transmission spectra of a 62 [cm] fiber-strand narrowband filter. The indicated full width at half-maximum (FWHM) of both spectra is 200 [MHz].

Even if this discovery contributed to grow up of fibers technology, the *self-induced* gratings did not find many usage because of their limitation and defects. First of all, the system used to realize them limits the grating spacing to the wavelength of the used laser. Furthermore, it has been observed that near the wavelength regions of green and blue the gratings are unstable and changes continuously while they are used. Another problem linked to the way of building this kind of gratings is the need to build long gratings if we want strong reflection due to the weak photoinducted refraction index change (Hill used a fiber 1 [m] long to obtain a $\sim$ 44% of reflection). In 1989 Meltz *et al.* [21] discovered a system to write Bragg gratings illuminating the fiber not internally but externally. They used a UV laser split in two beams. Each beam was launched onto the fiber in order to have the interference region in correspondence to the core. Tanks to this new system they overcame the problems earlier listed: this was the first system in which the grating period did not depend only from laser wavelength, but, in this case, also from the angle between the two beams as we can see in the Fig. 2.3 from Meltz's paper.

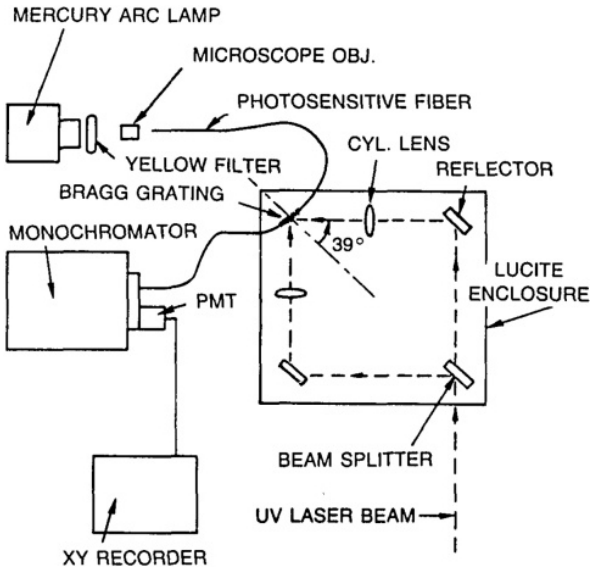

Figure 2.3: Figure number 1 from Meltz's paper [21]. Diagram of the experimental setup. A beam splitter (not shown) at the fiber input end is used with the monochromator to measure the reflection spectrum of the Bragg grating. PMT: photomultiplier tube.

2.3 Realization of FBG

Tanks to the work of Meltz and his team the interest in fiber Bragg gratings grew up and hence, during the five years after their publication, the main techniques to realize a FBG were developed: Interferometry, Phase Mask and Point-by-point.

2.3.1 Interferometry

This is the technique used by Meltz. Using this method there are two ways to get the interference necessary to inscribe a grating in the fiber: the *amplitude-splitting* and the *wave-front-splitting* [17].
The amplitude-splitting (Fig. 2.3) provides a division of the laser beam in two equal intensity beams and later a recombination of these beams that realizes the interference pattern. The main advantage of this system is the possibility of creating gratings with any pattern period changing the recombination angle between the two splitted beams. Nevertheless, this system has a non negligible defect: the high dependence to the position and alignment of the optic elements, indeed even a movement smaller than one micrometer can sensibly change the grating.
The wave-front-splitting could be realized by two different system: using a prism [22, 23] or using a Lloyd's interferometer [24]. In the first one a prism Fig. 2.4a is used to expand the beam when it comes in to the prism and, through internal total reflection, flips half of it in order to have the interference at the exit. The second employs a mirror Fig. 2.4b placed orthogonally to the fiber. The laser beam is centred at the intersection between the mirror and the fiber. With this set up half beam is directed on the fiber and the other half on the mirror. This half is reflected on the other and both form the interference that generates the grating. This system use only one optic element so the error probability coming from the set up is half compared to the split method. But, on the other hand, in this case we have

two limitation: a limited length range for the grating period and a higher attention to the coherence length of the laser beam. In the previous case we can neglect this last condition if we see that the total number of reflection are equal in both split beams. With these three methods the period of grating is given by

$$\Lambda = \frac{\lambda_s}{2\sin(\phi)} \tag{2.1}$$

where λ_s is the source wavelength and ϕ is the half-angle between two beams radius that generate the interference, as it is sown in Fig. 2.3 (the angle of 39^o) and Fig. 2.4

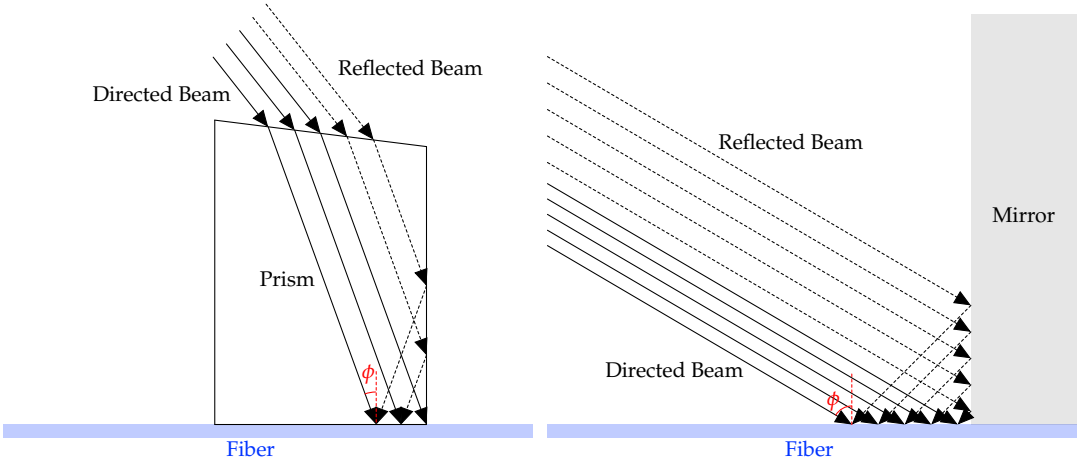

(a) Split Interferometer (b) Lloyd Interferometer

Figure 2.4: Schemes of the two interferometric techniques

2.3.2 Phase Mask

The most used system to create a FBG is the Phase Mask (PM) [25] technique. The PM is typically formed by a silica plate on a side of which, by a photolithographic process, a periodic pattern is realized [19].

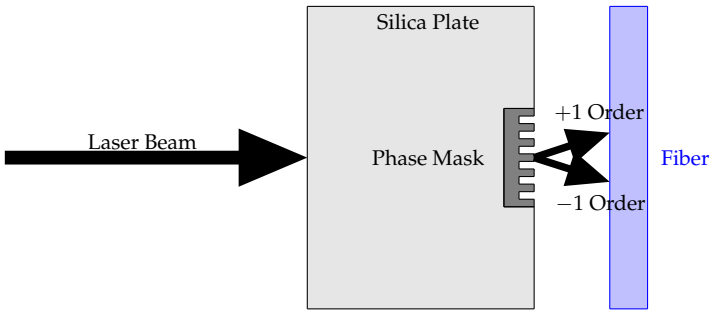

Figure 2.5: Description of the Phase Mask techniques

As we can see in Fig. 2.5 The set up for this FBG realization method is simple: a UV laser is launched on the phase mask and that is located in front of the fiber. Fiber and mask,

are orthogonal to the beam direction. The phase mask diffracts the laser light and at the same time suppresses the 0 order of diffraction, thereby only the ± 1 orders reach the fiber. Because of this, the period of the photoimprinted gratings is half then the mask one.

$$\Lambda = \frac{\Lambda_s}{2} \tag{2.2}$$

As we can deduce from the previous description, the system is simple but can guarantee high quality gratings. Another quality, linked to this peculiarity, is that it does not need the same precision and stability in the set up, comparing to the other system, and we can use a laser with a lower coherence length without any loss in the grating quality. A drawback using the phase mask is that the spatial periodicity of the FBG depends only from the mask periodicity that is fixed for every mask, so if we want to change the Bragg Wavelength value, we must change the mask. Apart from the already cited qualities, what makes this the most used technique in making FBG is the phase mask capability of creating different kind of gratings. An example of this is the *apodization*, a procedure that suppress secondary maxima of reflection. This effect can be got by appropriate changes in the standard FBG by combining the first two phase mask diffraction order (except 0) [26]. Moreover, using mask with a pattern lithographed not like a square wave but with a non zero angle against the normal to the silica plate side, we can create tilted or blazed gratings.
Another similar system less used, is the mask image projection [27]. It consists in photoinscribing the FBG copying the mask grating.

2.3.3 Point-by-point

Another system to build a FBG is the Point-by-point technique [28]. As suggested by the name, this technique consists in writing the bragg mirror one point after the other: a laser passes through a slit and is focused by a lens on the fiber core. When the first photoimprinting is completed, the carriage on which the laser, the slit and the lens are, shifts parallel to the fiber as long as the period of the grating that we want [17].

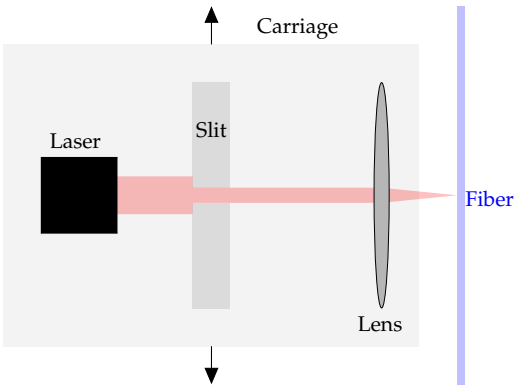

Figure 2.6: Schematic example of point-by-point technique

This system allows to easily create FBG with any kind of period: constant or variable in order to have a classic FBG or a chirped one or similar. However, a procedure like this needs a long time to be completed. Furthermore this procedure is strongly affected by errors due to imperfect alignment of the optic system and to a possible irregularity in translations steps.

2.4 FBG optical features and application

2.4.1 FBG optical proprieties

The simplest fiber Bragg grating is a periodic change of the core refraction index orientated perpendicularly to fiber direction. In Fig. 2.7 we can see a scheme of this kind of FBG. From now on, unless different specification, with FBG we mean this kind of FBG.

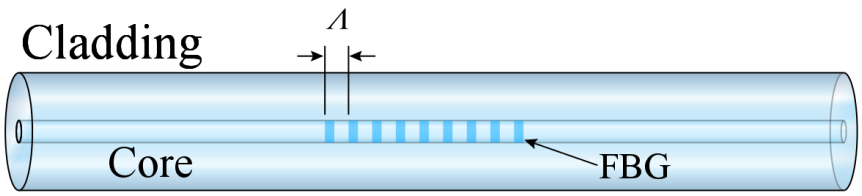

Figure 2.7: Scheme of a FBG

A Bragg grating sensor works as a stop-band filter [29]. By the conservation of energy and momentum we obtained the Bragg condition:

$$\lambda_B = 2n_e\Lambda \tag{2.3}$$

where λ_B is the wavelength reflected by the gratings, n_e is the effective core index of refraction and Λ is the grating period.

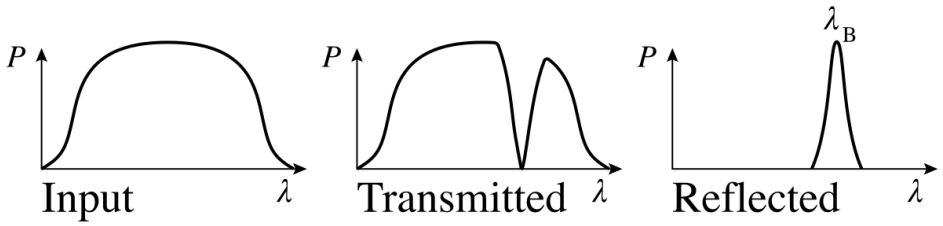

Figure 2.8: Typical wavelenght spectrum due to a FBG

There are several theories and modelling, principally based on the Coupled-mode theory [30], that describe the FBG optic proprieties. This is an approximated theory that treats the FBG as a combination of different simple waweguides that interact and perturb each other. Using this approximation the n_e in Eq. 2.3:

$$n_e(z) = n_0 + \delta n \cos\left(\frac{2\pi z}{\Lambda}\right) \tag{2.4}$$

where n_0 is the unperturbed refractive index of the core, δn is the perturbation amplitude and z the distance along the core axes. Using the Coupled-mode theory we can also calculate an analytical expression for the reflectivity [31]. This kind of calculus is based on the driving and the contropropagating mode that travel into the FBG. The differential equations that

describe these behaviour are

$$\frac{\partial A_\nu}{\partial z} = -iA_\nu k_{dc} - ik_{ac}^* B_\mu e^{i(\Delta\beta z - \phi(z))} \tag{2.5a}$$

$$\frac{\partial B_\mu}{\partial z} = iB_\mu k_{dc} + ik_{ac} A_\nu e^{-i(\Delta\beta z - \phi(z))} \tag{2.5b}$$

with

$$\Delta\beta = \beta_\mu + \beta_\nu - \frac{2\pi N}{\Lambda} \tag{2.6}$$

$$k_{ac} = \frac{\pi a N A}{\lambda} k_{dc} \tag{2.7}$$

- A_μ and B_ν are the driving and contropropagating modes amplitude
- μ and ν are the modes order
- k_{dc} and k_{ac} are the coupling coefficients
- β_μ and β_ν are the modes wave vectors
- N is the number of mirror in the grating
- Λ is the distance between two different mirrors
- NA is the fiber numerical aperture
- a is the core radius
- λ is the light wavelength
- $\phi(z)$ is an arbitrary spatial varying phase change

To solve the Eq. 2.5 we make the following substitution

$$R = A_\nu e^{-\frac{i}{2}(\Delta\beta z - \phi(z))} \tag{2.8a}$$

$$S = B_\mu e^{\frac{i}{2}(\Delta\beta z - \phi(z))} \tag{2.8b}$$

Differentiating Eqs. 2.8 and substituting into Eqs. 2.5 we get a new couple of equations

$$\frac{dR}{dz} + i\left[k_{dc} + \frac{1}{2}\left(\Delta\beta - \frac{d\phi(z)}{dz}\right)\right] R = -ik_{ac}^* S \tag{2.9a}$$

$$\frac{dS}{dz} - i\left[k_{dc} + \frac{1}{2}\left(\Delta\beta - \frac{d\phi(z)}{dz}\right)\right] S = ik_{ac} R \tag{2.9b}$$

Considering that for a standard grating $\frac{\phi(z)}{z} = 0$ we can solve Eqs. 2.9 with standard techniques. The boundary conditions are: at the input of the fiber grating the input signal has the maximum amplitude so at $z = 0$ $R(0) = 1$, on the other side, at the end of grating, because of the reflected signal can not overcome the grating we have at $z = L$ $S(L) = 0$. Finally, we get the FBG reflectivity evaluating the ratio between the input signal and the reflected one.

$$\Re = \left(\frac{S(0)}{R(0)}\right)^2 = \frac{|k_{ac}|^2 \sinh^2(\alpha L)}{|k_{ac}|^2 \cosh^2(\alpha L) + \delta^2} \tag{2.10}$$

Where L is the grating length,$\delta = k_{dc} - \frac{\Delta\beta}{2}$ and $\alpha = \sqrt{|k_{ac}|^2 - \delta}$. The peak of reflectivity occurs at a wavelength at which $\delta = 0$, consequently $\alpha = k_{ac}$ and Eq. 2.10 reduces to

$$\Re = \tanh^2(k_{ac} L) \tag{2.11}$$

Eq. 2.11 confirm what Hill observed [18], namely that the reflectivity of a FBG increases with the length of the grating and with the growing of the refractive index alteration. To confirm the goodness of this method we report from the paper of Hill and Meltz [29] the figure number 5 and its caption Fig. 2.9

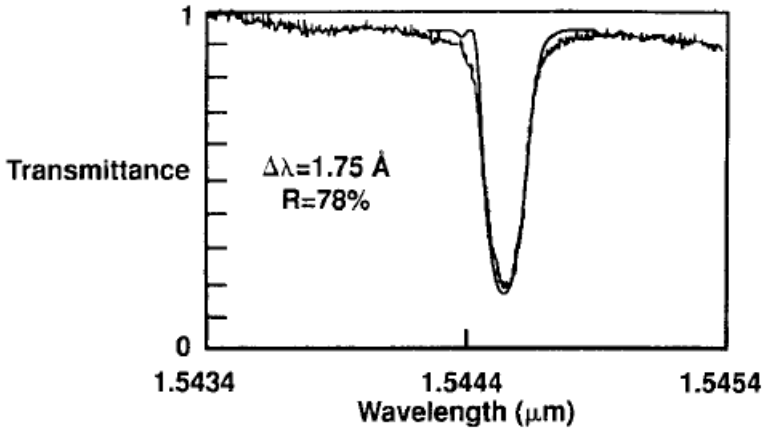

Figure 2.9: Comparison of computed and measured transmission spectra for a moderate reflectivity Gaussian-apodized fiber grating. The grating length is about 10 [mm] as determined from measurements of the approximately Gaussian UV beam width; the grating strength ($\delta n/n = 9 \cdot 10^{-5}$) was inferred from the measured minimum transmittance.

2.4.2 FBG as optical devices

The simplest kind of device that we can build using a FBG is the FBG itself: as we already said the FBG acts like a **band rejection filter**, see Fig. 2.8. This filter can be achieved using FBG with bragg planes orthogonal to the core axis or tilted against it. In the first case, the filter, back reflects the portion of signals removed from the input one. In the second one this part of signal is reflected outside of the core. The complementary device, **bandpass filter**, can be achieved combining an optical circulator with the FBG how is shown in Fig. 2.10

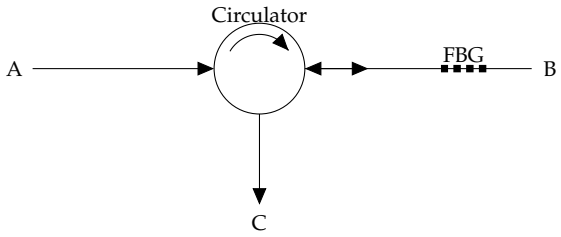

Figure 2.10: Schematization of a circulator: signal comes from channel A goes to B and the reflected part comes back to circulator and goes to C

Another configuration of this kind of device can be realized using a Mach-Zehnder interferometer and two fibers couplers
This configuration can be used also as **optical add-drop filter** [32, 33]. Devices like this are much used in telecommunication field due to their features of low-loss signal and high stability.

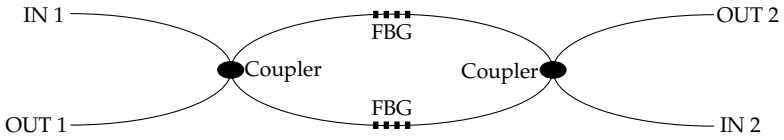

Figure 2.11: Schematization of a Mach-Zehnder interferometer: signal comes from IN 1 goes to both FBG and the reflected part come back to OUT 1, instead trasmitted signal goes to OUT 2 and to IN 2. The device has a symmetric behaviour if we change the imput from IN 1 to IN 2

If we place two identical FBG sequentially in a fiber, we get an in-fiber **Fabry-Perot** that with today technology can have finesse higher than several thousands.
Another use of a sequence of FBG is that shown in the work of Reekie *et al*. [34]. They realised a **FBG Laser** by doping the core of a fiber 2 [m] long with Er^{3+} and writing a sequence of five FBG. In this way they obtained the same effect of a resonating cavity, getting an output power of $5[\mu W]$ against the $3[mW]$ input one.
Tilting a grating of $\sim 1^\circ$ against the core axis Hill *et al*. [35] realized a **spatial-mode couplers** able to switch from the fundamental mode LP_{01} to higher order LP_{11}
With a similar technique, a year later, Hill and his team [36] built a **polarization mode converter** (also called **rocking filter**).
Finally, another use of FBG as optical device is that demostrated by Eggleton *et al*. [23] and then realized Williams *et al*. [37]: the **dispersion compensation device**. In these works they have shown how to use a chirped FBG (a FBG with a variation in the grating period) as a pulse compressor in order to compensate the chromatic dispersion due to the travelling through kilo-metric distances.

2.5 FBG as sensors

The extreme sensitivity of a FBG to external conditions make it a great sensor. Even the littlest variation that changes somehow the grating, affects the FBG response in term of the reflected wavelength. This kind of usage of a FBG finds application in several fields for different kind of measurements: the principal one is the civil engineering. The reflected wavelength is a function of (Eq. 2.3) distance between two grating planes (Λ) and the effective refraction index (n_e) (which also depend upon Λ Eq. 2.4). Apart from chemical events that could change the elements parameters, the variations that influences Λ are thermal gradient or compression/dilatation. These two things can be linked to the reflected wavelength by simple mathematical steps. Differentiating Eq. 2.3 we get [6, 38]

$$d\lambda_B = 2\Lambda dn_e + 2n_e d\Lambda = 2\left(\Lambda\frac{\partial n_e}{\partial l} + n_e\frac{\partial \Lambda}{\partial l}\right)dl + 2\left(\Lambda\frac{\partial n_e}{\partial T} + n_e\frac{\partial \Lambda}{\partial T}\right)dT \tag{2.12}$$

now dividing Eq. 2.12 by Eq. 2.3 we get

$$\frac{d\lambda_B}{\lambda_B} = \left(\frac{1}{n_e}\frac{\partial n_e}{\partial l} + \frac{1}{\Lambda}\frac{\partial \Lambda}{\partial l}\right)dl + \left(\frac{1}{n_e}\frac{\partial n_e}{\partial T} + \frac{1}{\Lambda}\frac{\partial \Lambda}{\partial T}\right)dT \tag{2.13}$$

The first couple of brackets of Eq. 2.13 is the member related to the length deformations, the second one is that related to temperature variations. We now analyse these separately starting from the first:

$$\frac{1}{n_e}\frac{\partial n_e}{\partial l}dl + \frac{1}{\Lambda}\frac{\partial \Lambda}{\partial l}dl \tag{2.14}$$

the first element of Eq. 2.14 describes the refractive index changes under mechanical stress, it can be write as $p_e\varepsilon$ where ε is the strain along fiber axis and p_e is the effective strain-optic constant defined as

$$p_e = \frac{n_e^2}{2}\left[p_{12} - \nu\left(p_{11} - P_{12}\right)\right] \tag{2.15}$$

with p_{11}, p_{12} components of the strain-optic tensor and ν the Poisson's ratio. Typically, these parameters values, considering an ordinary silica fiber, are: $p_{11} = 0.113$, $p_{12} = 0.252$, $\nu = 0.16$ and $n_e = 1.482$. This effect is negative, indeed an expansion of the FBG causes a decrease in the refraction index value, due to the decrease of the material density, and consequently a negative wavelength shift. So Eq. 2.14 becomes

$$\frac{1}{n_e}\frac{\partial n_e}{\partial l}dl + \frac{1}{\Lambda}\frac{\partial \Lambda}{\partial l}dl = -p_e\varepsilon + \frac{1}{\Lambda}\frac{\partial \Lambda}{\partial l}dl \tag{2.16}$$

dividing and multiplying the second addend by the total fiber length L_f we get

$$-p_e\varepsilon + \frac{1}{\Lambda}\frac{\partial \Lambda}{\partial l}\frac{L_f}{L_f}dl = -p_e\varepsilon + \frac{\partial \Lambda}{\Lambda}\frac{L_f}{\partial l}\frac{dl}{L_f} \tag{2.17}$$

the first and the third ratio of the last element in Eq. 2.17 are, respectively, the strain of grating ε_g and of the fiber ε_f, while the second one is reciprocal of the fiber strain. Since the grating is in the fiber, all of these strain are the same strain $\varepsilon_f = \varepsilon_g = \varepsilon$. So we can write

$$\frac{1}{n_e}\frac{\partial n_e}{\partial l}dl + \frac{1}{\Lambda}\frac{\partial \Lambda}{\partial l}dl = -p_e\varepsilon + \varepsilon = (1 - p_e)\varepsilon \tag{2.18}$$

$$\frac{d\lambda_B}{\lambda_B} = (1 - p_e)\varepsilon + \left(\frac{1}{n_e}\frac{\partial n_e}{\partial T} + \frac{1}{\Lambda}\frac{\partial \Lambda}{\partial T}\right)dT \tag{2.19}$$

The last brackets in Eq. 2.19 contain the terms linked to the thermal variation. The first one is the thermo-optic coefficient γ (that is $\sim 6 \times 10^{-6}\ ^\circ\mathrm{C}^{-1}$ for fused silica fiber), the second one is the fiber thermal expansion coefficient α (that is $\sim 0.55 \times 10^{-6}\ ^\circ\mathrm{C}^{-1}$ for silica fiber). Tanks to these considerations we can write

$$\boxed{d\lambda_B = \lambda_B(1 - p_e)\varepsilon + \lambda_B(\gamma + \alpha)dT} \tag{2.20}$$

Eq. 2.20 makes possible to link the wavelength behaviour to external causes. Using the already cited parameters value for a Bragg gratings with a wavelength centred at $\sim$ 1550 nm we have a shift in wavelength of 1.2 pm/$\mu\varepsilon$ caused by strain and 10.2 pm/$^\circ$C by thermal variations.

The simplest possible uses of FBG as sensors are **strain gauges** [39] and **thermometers**. The first is easy convertible to a **pressure meter** or **force meter**, indeed from the strain calculation of a particular object it is easy to evaluate the force, or the pressure, that generated it.

With an appropriate system to convert external stimulation to strain, we can use the FBG to measure several kinds of physics quantities, e.g. covering the fiber, at the FBG site, with a magnetostrictive element make the FBG a **magnetic field sensor** Fig. 2.12. This particular material in presence of a magnetic field extends or contracts itself. Glueing it to a FBG the deformation is handed over to the grating and we can measure the magnetic field by the wavelength shift.

With an appropriate transducer many other physical parameters can also be measured such as **flow** [41]. Embedding the fiber near the FBG like shown in Fig. 2.13 we are able to make

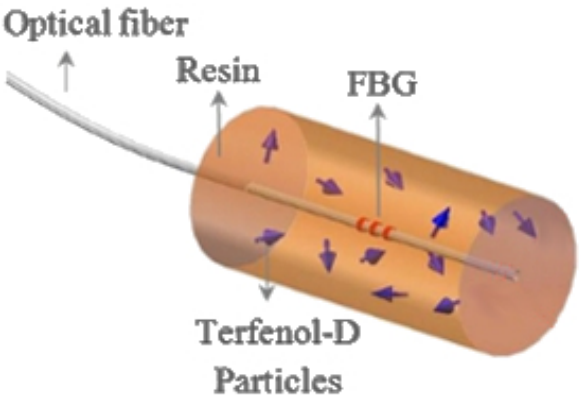

Figure 2.12: Part of figure number 4 from Quintero's paper [40]. Example of a magnetic field sensor.

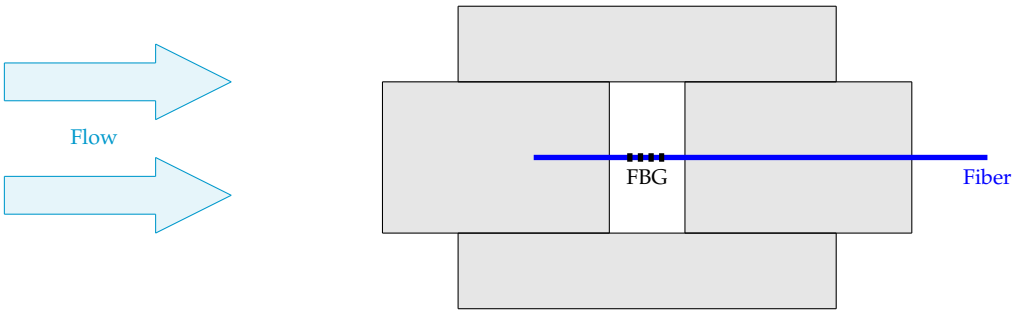

Figure 2.13: Scheme of a FBG flow meter. The lateral tops move themself following the fluid flow and hand over the stress to the FBG.

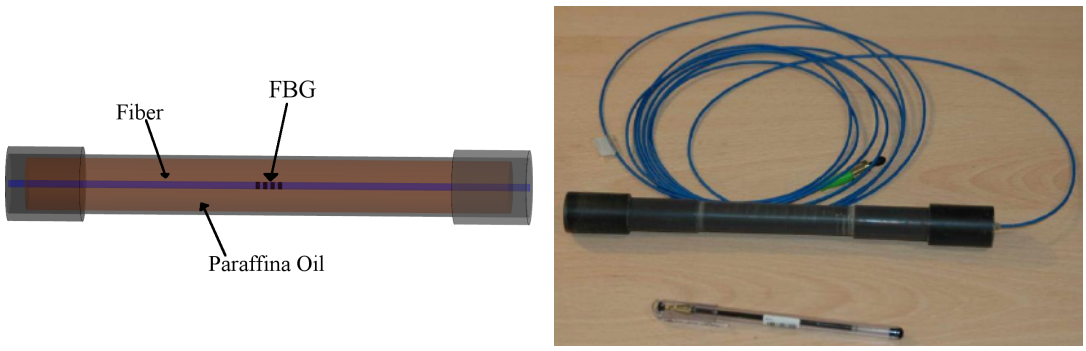

(a) Scheme of the FBG hidrophone (b) Photo of a bilded one

Figure 2.14: Scheme and photo of a FBG hidrophone realized by Beverini *et al.* [42]

this kind of measure. The lateral protections prevent from noise due to random fluctuation of the fiber in the fluid.
Another similar set up is used to build a **underwater acoustic sensor** (**hydrophone**) Fig. 2.14. The encapsulation schematised in Fig. 2.14a is realised to prevent from noise due to random fluctuation and to sense the acoustic wave.
A last example of FBG sensor type is the **accelerometer** [43]. This is realized gluing the FBG to a cantilever that has one extremity blocked and the other pasted to a free mass. The

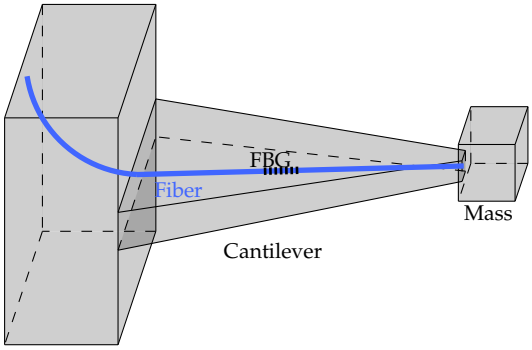

Figure 2.15: Schematization of a FBG accelerometer

gravity acts on the mass that stretches the FBG bending the cantilever.

2.6 Embedded FBG

An additional and non negligible function of encapsulation is fiber protection, bare silica fibers are extremely fragile. Typically, this function is carried out by the cladding layers but if we submit fibers to strong stresses they could break.Usually a fiber can hold up stress of a few milli-strain and can be bent to a curvature radius of 5 [cm]. Higher tensions or torsions can take to the lost of the elasticity propriety or worse to the breakage. In both cases Eq. 2.20 loses its validity and the fiber becomes useless. Fiber Bragg sensors are largely based on the conversion of external stimulations into a strain, some of this could be higher than the fiber resistance. To avoid it the protection must be designed every time in function of the measurements that we are going to do. There are several studies [5, 6, 44] about the techniques to encapsulate fiber. Generally the protection cover a length of $\sim$ 10 [cm] centred on the FBG while the remaining part of the fiber is protected by cladding or by a second type of encapsulation like a Teflon tube or similar. For example in civil engineering FBG are massively used as strain gauges sensors. In this case the typical encapsulation is a steal tube welded to two discs as we can see in Fig. 2.16

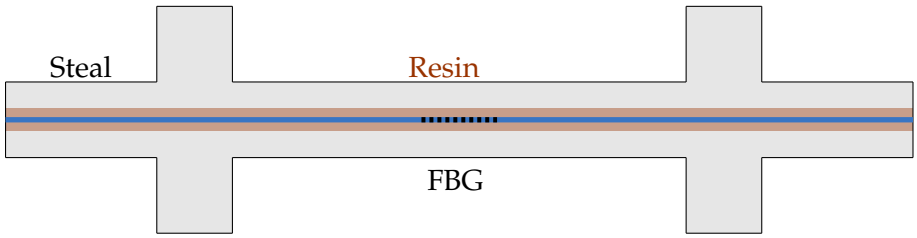

Figure 2.16: Scheme of an embedded FBG

In order to maximize the connection among the steal and the FBG, typically is used a metallic resin. This kind of resin has an important peculiarity: when it solidifies it gets mechanical proprieties similar to a metallic element. The two discs act like an anchor, to keep in position the sensor, and at the same time to guarantee that it could follow the movements of the mass in which it is inserted.

CHAPTER 3

Building of the Sensor

3.1 Characteristics and idea of the sensor

FBG sensors are widely used in civil engineering, but recently these sensors found applications also in geological research field. Indeed, in 2001 Ferraro and De Natale [9] have shown how these devices can be used for geological measurements. Afterwards, J. R. Moore *et al*. [10] and Z. He *et al*. [11] used these sensors in their experiment of rockslide deformation monitoring and crustal deformation measurement. Until now these kinds of sensors have been used to measure the movements between the two sides of a fault, whereas we will use them to measure the movements of a rock block generated by volcanic activity. We are planning to realize a tri-axial cheap strain sensor able to measure rock movements along the three Cartesian axes and identify amplitude and direction of perturbation. By choosing an FBG as strain sensor we can satisfy the request of low cost and, with an appropriate interrogation system, we could obtain both the resolution and the dynamic range that we need. Therefore, issues that we have to solve are: realizing our sensor in a *small volume* together with the interrogation system that we need. The request of a small sensor is due to the reduced available space in the installation site. Indeed, the measurements must be performed at $\sim 10\,[\mathrm{m}]$ underground, hence we are forced to put the sensor at this depth. The system that we will use to reach this depth is based on the technique used to dig artesian well, therefore once the borehole is made its width can not be modified. Our drill can dig boreholes with a diameter of $150 \div 200\,[\mathrm{mm}]$ and hence, in order to be sure that we can lower the sensor and fix it to the bottom, we work as this diameter is only $100\,[\mathrm{mm}]$ long. Taking into account these considerations, we plan to encapsulate our FBG sensors in a concrete cylinder in order to exploit the available space in the best possible way.
Instead, the main difficulty related to the interrogation system is to choose suitable optical, electro-optical and electronic components. FBG can detect all kinds of movements that change the spacing between Bragg mirrors. Our interrogation system must be able to reach it through the wavelength shift. Moreover, the location were we are going to work is electrical isolated and is also unattainable during the period starting from November until the end of March. Therefore, all the systems must be powered by solar panels and batteries.

3.2 Sensor design

We have designed and then realized the system of optical fibers and FBGs in laboratory.

When it was ready, we have walled it up in concrete cylinder with a diameter of 100 [mm] and a height of 335 [mm]. The selected concrete is the **Mapegrout Colabile**, a product of Mapei S.p.A. This concrete has been chosen thanks to its similarity, in terms of mechanical properties, to the basalt rock in which the borehole is going to be dug. Both of these elements have similar Poisson's ratio $\nu_{conc} = 0.2$, $\nu_{bas} = 0.25$ and similar Young modulus $E_{conc} = 70$ [Gpa], $E_{bas} = 75$ [Gpa]. In addition to already said motivations Sec. 3.1, choosing to build up the cylinder in laboratory simplifies the lowering process and let us able to make stress tests on the FBGs inside a material comparable to basalt rock.
At the beginning the small volume in which we have to work seemed a hard task. The metallic protection for the FBGs that we have developed was too long (see Fig. 3.1) to use a Cartesian configuration of sensors with horizontal and vertical axes.

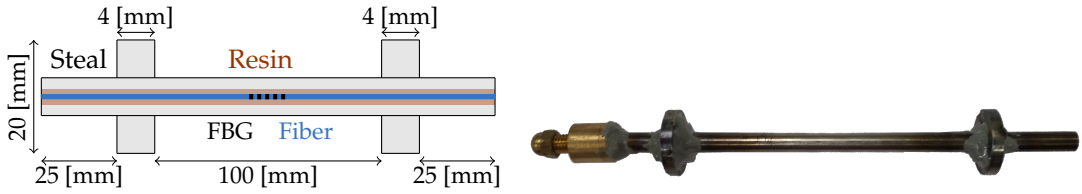

(a) Section

(b) Image

Figure 3.1: Protection for FBG

This protection was described in Sec. 2.6, in this case the welding between tube and rings is made by a metallic glue. On the left side of the tube in Fig. 3.1b is welded a clamp that keeps the fiber blocked during the process of gluing it to the metallic tube. Due to the technique used to connect the fiber containing the FBG, this is the shortest cover realizable. Indeed, to merge the fibers we have to remove all protection layers of a large part of them. To be sure that the fiber is protected in this zone we use an encapsulation like Fig. 3.1, that covers all of fiber unprotected zone.

3.3 20 degree sensor

Before changing the merging technique or the protection type, we try to use this embedded FBG in different configuration from the Cartesian one with horizontal and vertical axes. First of all it is important to note that the previous design is perfect for a vertical sensor. In vertical direction there are no dimension limits and the sensor sensibility to vertical stimulations is maximized. Starting from this consideration, we put the embedded FBG not along the vertical axis but with an angle of 20° against it Fig. 3.2.
The FBG works as strain gauge mainly along the fiber direction, all kinds of stretches or compressions coming from directions orthogonal to the fiber one are lessened by the steel cover. These stresses can be sensed because of the *Poisson effect* Fig. 1.5 anyway. Considering this we are able to measure all kinds of stresses even if we keep the FBG vertically, but, on the other hand, due to the system symmetry, we can not discern what kind of stress we are measuring. Only vertical stresses, acting along the sensor direction produce a larger wavelength shift could be identified. To solve this problem we asymmetrize the configuration using the one that is shown in Fig. 3.2. Even if is still present the *Poisson effect*, now we have two axes directly sensible to the stress. Using goniometric laws we can decompose

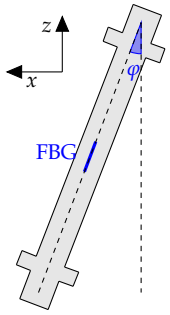

Figure 3.2: First tryed configuration

all perturbations parallel to the plane zx (as shown in Fig. 3.2 we have described the plane with the Cartesian axes x and z) in a longitudinal and a transversal component to the grating direction. Unfortunately this configuration has an intrinsic and unsolvable problem: the equations system that we have to solve to calculate the strain on both axes has two equations but three variables.

$$\begin{cases} \varepsilon_z = \varepsilon_s \cos(\varphi) \\ \varepsilon_x = \varepsilon_s \sin(\varphi) \end{cases} \tag{3.1}$$

In addition to ε_x and ε_z also φ depends on the stress that compress or stretch the sensor. The encapsulation is built to follow the movements of what is around it, this means that nothing in the sensor geometry stays fixed during a stress Fig. 3.3.

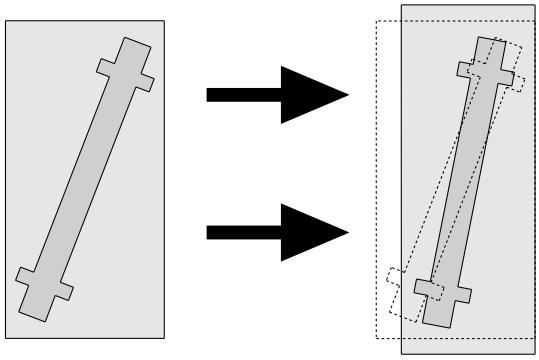

Figure 3.3: Example of lateral force effects on the sensor in a concrete cylinder

Initially, considering that the strain values which we expect are smaller than 50 $[\mu\varepsilon]$ (that means a compression with magnitude of 0.005% of total length), we have tried to solve Eq. 3.1 assuming φ as a constant. Through finite element simulation, we have modelled a sensor like the one in Fig. 3.2 walled up in a concrete cylinder and then we have simulated vertical and horizontal compressions. These simulations let us able to check if the estimation of Eq. 3.1, approximating φ as a constant, is consistent with the real vertical and horizontal compressions. Unfortunately these data, and those coming from strain tests showed too many incongruities. We have also tried to solve Eqs. 3.1 using the Poisson's ratio Eq. 1.4. But also this value does not help us, since we can use it only if the force direction, that generate the compression, is along x or z axis, in other cases we can not use this value.

3.4 Circular sensor

The problems found with the previous disposition took us to design a completely different sensor configuration. We chose to use the previously described sensor only for vertical axis, hence we focused to find a system able to measure only horizontal stresses. This idea simplifies the problem reducing it from 3D to 2D. To build the second type of sensor we have tried to use as much as possible the cylinder circular symmetry, and the information of the Poisson's ratio. Our idea was that every kind of lateral force, with the same intensity, deforms the cylinder in the same way. Moreover, the only thing that changes varying the force intensity is how much the deformation is emphasised. The new sensor, based on these hypotheses, was realized gluing the bare fiber to a steel thin cylinder used as concrete container. In order to protect the fiber and strongly fix it to the cylinder, we use a metallic resin. In this case the fiber has two different FGB placed at 90° each other as it is shown in Fig. 3.4.

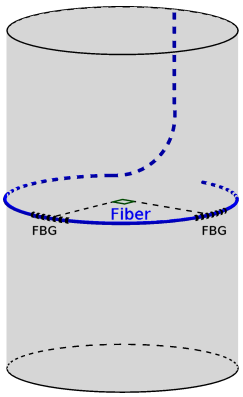

Figure 3.4: Scheme of circular sensor

Following our hypothesis the cylinder circular form, exposed to lateral stress, should become an elliptical one. We have made one more hypothesis: due to the small deformations

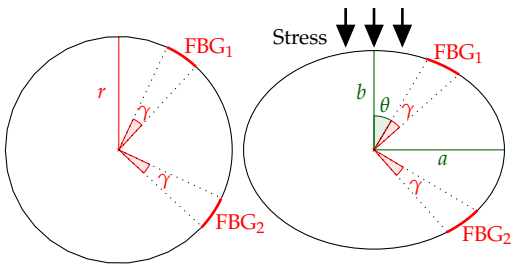

Figure 3.5: Example of the deformation hypotized

expected (less than 0.005%), the angle subtended by the FBG (γ in Fig. 3.5) keep constant. Starting from the measured strain by FBG we try to calculate the value of ellipse axes and the angle between one of the FBG and the stress direction (b a θ see Fig. 3.5). In this way we are able to determinate the stress direction (thanks to θ) and its intensity (thanks to strains of b and a). Obviously, all of these calculi must be integrated with data got by the vertical sensor in order to have a complete description of the phenomena. The problem is also sim-

plified by the Poisson's ratio. Thanks to the direction of ellipse axes[1] we can use this value to link the axes. In terms of equations we have to solve:

$$\begin{cases} L_1 = a \int_{\theta}^{\gamma+\theta} \sqrt{1 - e^2 \sin^2(x)} dx \\ L_2 = a \int_{\theta+\frac{\pi}{2}}^{\gamma+\theta+\frac{\pi}{2}} \sqrt{1 - e^2 \sin^2(x)} dx \\ \nu = -\dfrac{\varepsilon_a}{\varepsilon_b} \end{cases} \tag{3.2}$$

where

- L_1 and L_2 are the final length of FBG
- ν is the Poisson's ratio
- $e = \sqrt{1 + \left(\frac{b}{a}\right)^2}$ is the elliptic eccentricity
- ε_a and ε_b the strain of elliptic axes
- $\gamma = \frac{L_{1_0}}{r} = \frac{L_{2_0}}{r} = \frac{L_0}{r}$

The first two equation of Eq. 3.2 are the so called *incomplete elliptic integral of the second kind* solvable only by approximation. Solving Eq. 3.2 we get

$$\varepsilon_a = \nu \frac{\nu(\varepsilon_1 + \varepsilon_2 - 1) + 1 - \sqrt{(\nu-1)^2 + \nu^2 (\varepsilon_1 + \varepsilon_2)^2 + 2(2\nu^2 + \nu + 1)(\varepsilon_1 + \varepsilon_2)}}{3\nu^2 + 1} \tag{3.3a}$$

$$\varepsilon_b = -\frac{\nu(\varepsilon_1 + \varepsilon_2 - 1) + 1 - \sqrt{(\nu-1)^2 + \nu^2 (\varepsilon_1 + \varepsilon_2)^2 + 2(2\nu^2 + \nu + 1)(\varepsilon_1 + \varepsilon_2)}}{3\nu^2 + 1} \tag{3.3b}$$

$$\theta = \frac{1}{2} \arccos\left(\frac{2aL_0 (\varepsilon_1 - \varepsilon_2) \nu^2}{\sin(\gamma)(\nu+1)(a-r)(a(\nu-1) + r(\nu+1))} \right) - \frac{\gamma}{2} \tag{3.3c}$$

A complete demonstration of Eqs. 3.3 is in App. A. Integrated with the vertical sensor, this could be the definitive configuration of a tri-axial sensor. Unfortunately experimental data, finite elements simulations and considerations on elements with which the sensor is constituted have shown that it is unusable. The under stress sensor behaviour was not like we have hypothesized. The force variation influences the deformation by generating an asymmetry. We have rightly hypothesised that the deformation form does not depend on the perturbation strength, and that it influences only the deformation intensity. Our mistake was to consider the force effect constant during the deformation process. Even if we found the error we can not fix it because the final form of the deformed cylinder can not be modelled by any geometric form. This kind of problem should become negligible when the cylinder is inside the borehole, the large dimensions of basalt rock around it makes the deformation more homogeneous. Unfortunately there is another important and unsolvable problem: the steel cover around the cylinder. This is used as external protection for the fiber but it has also a collateral effect: the introduction of a discontinuity layer. Once the sensor is walled up into the borehole, the steel cover breaks the continuity between rock and concrete and that could influence the measurement. In addition to this, during the experimental test,

[1] For each compression they are one parallel and the other orthogonal to the compression direction

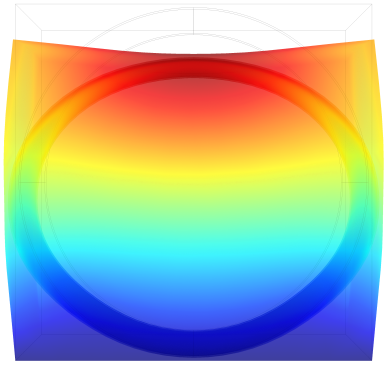

Figure 3.6: This is the result of the compression of cylinder inside a parallelepiped of basalt rock larger than the cylinder diameter of 2 [cm]. In this case we have intentionally emphatized the deformation to better show the described asymmetry.

sensors have shown another drawback due to the technique used to glued the fiber to the steel. During the resin solidification, or it application, the fiber is not fixed, so it could lose the adherence with the steel layer. This imperfect positioning of fiber could generate false signals or huge errors during the measure.

3.5 Cartesian sensor

The failure of the two previous tests, take us to consider that the only available way is to use a Cartesian configuration. The great advantage in using this kind sensors disposition is the direct measure of diagonal elements of strain tensor. In this way our sensor measures the relative elongation (or contraction) along three axes mutually orthogonal directly, without needing any kind of signal processing.
Nevertheless, we still have to solve the problem of small usable volume. To do this, we have used a middle way between the techniques earlier described. The new protection design for horizontal sensors, is the same of the one used for the z sensor, but, obviously, smaller than this. In this way the encapsulation covers the FBG and a little part of bare fiber near it. The residual one must be protected with a different system. We can not cover it with the metallic resin, as we have done for the circular sensor. It is a strong protection, but it limits too much the fiber movements, causing problems during the set up phase. We choose to close it in a Teflon tube of 4 [mm] of external diameter and 3 [mm] of internal one. In order to protect the bare fiber and, simultaneously, allow us to bend it without breaking risks.
As it is shown in Fig. 3.7, apart from the dimension, the new small encapsulation presents another difference compared to the bigger one. In order to make easier the realization and the combination with the others sensors. In this case the discs are welded as tops of the metallic tube.
To assemble these three sensors in the better possible way we have made several simulations, each one with a different sensors configuration: one above the other, the long one along the cylinder axis and the others two on the plane at middle height of cylinder. In order to simulate as the best we can the sensors working condition, we have simulate the compression of a cube of basalt rock of 20x20x20 [m], containing, in its center, the concrete cylinder with the sensors. All of these configurations have shown equivalent behaviour during all simulated compression, so we have chosen the one which allows to the horizontal sensors fibers the largest possible space. In this way we avoid too much narrow curvature radii.

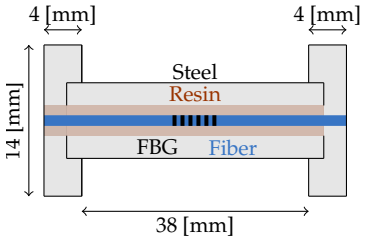

(a) Short sensor dimension

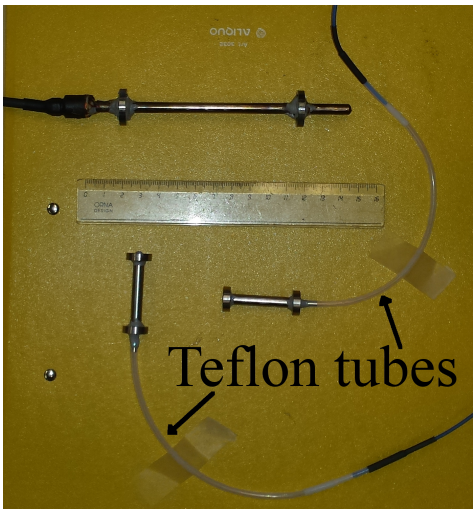

(b) Comparison between sensors

Figure 3.7: The 3 sensors used

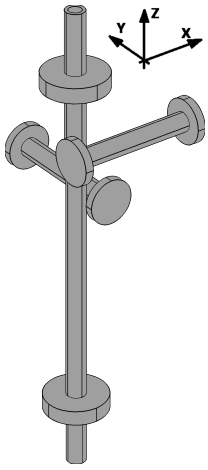

(a) 3D model

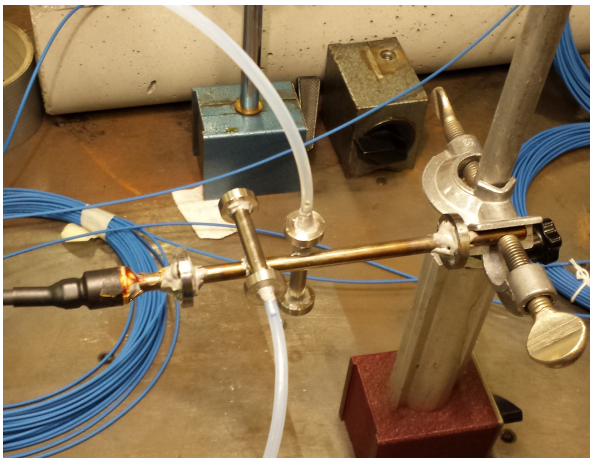

(b) Configuration photo

Figure 3.8: The chosen configuration

Once the three sensors are assembled, they must be walled up in the concrete cylinder. This is made using an empty PVC cylinder in which the sensors are positioned by fishing lines. During all the phases of concrete insertion and it solidification, our sensors system must preserve its initial position. To satisfy this request we have welded the short sensors to the long one. The welding point covers a sufficiently little part of sensors tubes so as not to influence the measurement.
A thermoresistor NTC 10K[2] and, on the top of the cylinder, two metallic rings (Fig. 3.9b) have been walled up into the concrete cylinder Fig. 3.9b. The two rings have been installed in order to simplify the lowering operations into the borehole. The NTC 10K is a thermometer, with a resolution better than 10^{-3} $[^{\circ}K]$, used as a landmark during temperature tests and

[2]Negative Temperature Coefficient of 10 kOhm

as a control sensor about the borehole temperature stability.
All of cables, both fibers and NTC electric cable, have been tied together and, inside a rubber tube, conducted to top of cylinder. We monitored the FBGs during all concrete solidification

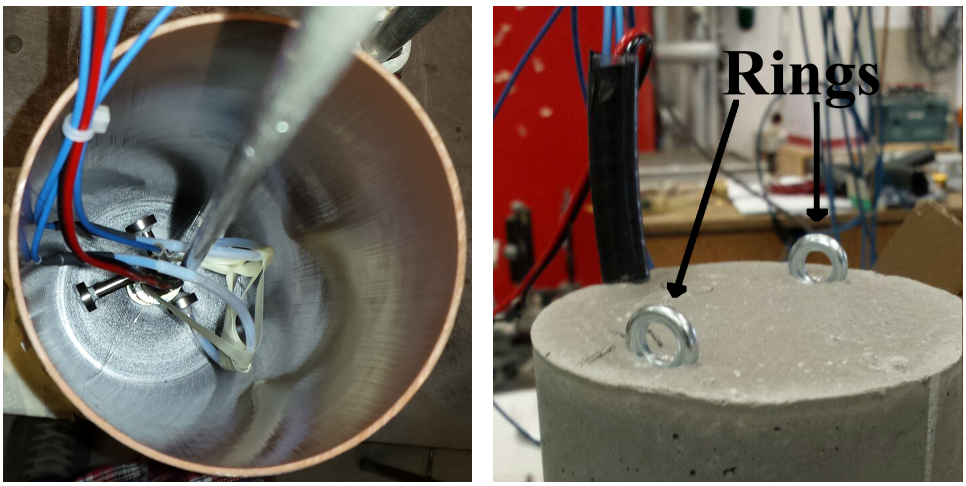

(a) (b)

Figure 3.9: Configuration of walled up sensors inside the empty PVC cylider and the final disposition of cables and rings on its top

period (about 4 weeks). The monitoring system was made by the **SmartScan**, a product of Smart Fibers Ltd. This device is specifically realized for FBG interrogation. It works as a source of light and as a scanner in a wavelength region of 40 [nm] (from 1528 [nm] to 1568 [nm]). Controlling it by a computer with its dedicated software, it can simultaneously monitor up to 16 FBGs. Thanks to the software, we can control the behaviour of the wavelengths reflected by FBGs, and register them using different acquisition rate. Moreover the software can be integrated with a custom LabVIEW source code modules, in order to refine the measurements.

3.6 Test on sensor and Simulation

Once the concrete cylinder has dried, we have removed the plastic cover and started the tests in order to verify the sensors operation and to calibrate them.

3.6.1 Temperature test

As we have seen in Sec. 2.5, FBGs is sensitive both to strains and temperature variations. In regard of temperature, the typical conversion value of 10.2 [pm/°C] works only for bare fibers. Steel protection and concrete container could change this value so we need to evaluate it again. The temperature test was made using a lamp to warm up cylinder temperature. During the heating we monitored sensors wavelengths and its internal temperature by the NTC. When the temperature has stabilized, we stopped the measure. The measurement has gone on for 8 $[h]$ 3 $[m]$ 20 $[s]$ with a data acquisition rate of 10 [Hz].
Following the theory (Eq. 2.20), we fitted the data with a linear function. Results in table

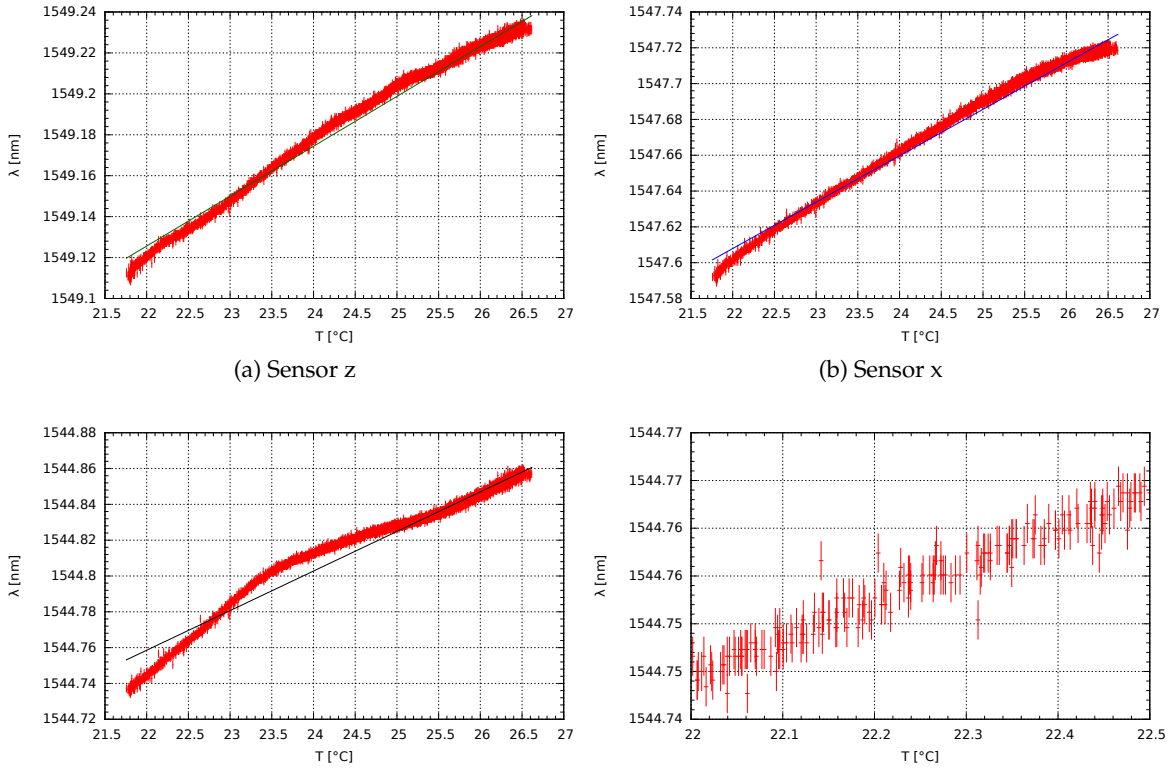

(a) Sensor z

(b) Sensor x

(c) Sensor y

(d) Zoom of sensor y

Figure 3.10: Sensors wavelength behaviour during temperature increase

Sensor	m [pm/°C]	Δm [pm/°C]	q [nm]	Δq [nm]
z	24.372	$5 \cdot 10^{-3}$	1548.5894	$1 \cdot 10^{-4}$
x	25.900	$5 \cdot 10^{-3}$	1547.0381	$1 \cdot 10^{-4}$
y	22.106	$8 \cdot 10^{-3}$	1544.2722	$2 \cdot 10^{-4}$

Table 3.1: Writing the straight lines equations of Fig. 3.10 as $f(x) = mx + q$ in this table are reported the m, q and their errors values

Tab. 3.1 show that the conversion factor between the temperature and the wavelenght is higher for an encapsulated fiber than for a bare fider. This effect is due to the thermal expansion coefficients of steel and concrete. As a matter of fact these factors are than thirty times the fiber one, about $12 \cdot 10^{-6}[°C^{-1}]$ for concrete and $24 \cdot 10^{-6}[°C^{-1}]$ for steel. During the temperature test, the thermal expansion of concrete and steel act on the fiber starching it, in this way the temperature-wavelength conversion factor of fibers increases.
In all of 3 cases showed in Fig. 3.10 the data series start under the fitted line, overcome it and after ~ 2 [°C] come back under it. For the y sensor this behaviour is more emphasised than the other two. This can be explained by presence of air bubbles, inside concrete or inside the resin between fiber and steel. These bubbles alter the normal heat flux and consequently the fiber responses to temperature variation. This anomalous behaviour is not a big trouble, because in the borehole at the working depth the temperature is around 10 [°C] and it is stable during all year in a range of ± 0.5[°C]. We will use this information in the future in order to help us in the construction of the sensor interrogation system.

3.6.2 Strain test

The main goals of these measurements and tests are: finding and evaluating the relation between force (or pressure) acting on the sensors and their wavelength shifts. The first part of Eq. 2.20 shows that the relation between wavelength shifts and strain is linear

$$\Delta\lambda_b = C_\varepsilon \varepsilon \tag{3.4}$$

where C_ε is the ratio between wavelength shift and strain. To do these tests we have followed the procedure of *simple compression*, in this way the stress tensor has an only one non zero element. If we call the the vertical direction, on which we compress the cylinder, z and the other two x, y we get

$$\sigma_{ij} \neq 0 \quad \Leftrightarrow \quad i = j = z \quad \rightarrow \quad \sigma_{zz} = p \tag{3.5}$$

where p is the applied pressure. Thanks to the relation between the tensor of stress and strain Eq. 1.5, during this type of compression also u_{ij} is diagonal. In this particular case the orientation of FBGs inside the concrete describes the same reference system in which u_{ij} is diagonal, hence by the inversion of Eq. 1.5 we have

$$u_{zz} = \varepsilon_z = \frac{1}{E}\sigma_{zz} = \frac{1}{E}p \tag{3.6a}$$

$$u_{xx} = u_{yy} = \varepsilon_x = \varepsilon_y = -\frac{\nu}{E}\sigma_{zz} = -\frac{\nu}{E}p \tag{3.6b}$$

where E and ν are the Young's modulus and Poisson's ratio of concrete.
To do these tests we have used an hydraulic press, able to compress with strengths up to 50 [kN], and the **SmartScan** to save wavelength values. Compression tests, with the same equipment and method, has been made also on the other two sensors configuration. Even if we have discarded them, these tests have been useful anyway. The information got about concrete reactions to the press have shown that we can not compress it with forces higher than 20 [kN]. Stronger forces could generate micro-fractures inside concrete and, consequently, anomalous sensors response.
Another problem found during previous tests is the inability to do valid radial compression test. Due to the curvature of lateral cylinder surface, to compress it along one of its radius we had to use a sort of clamps.

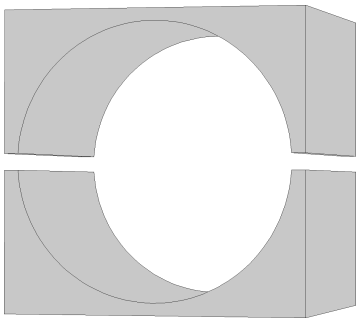

Figure 3.11: Schematization of the radial clamps

These clamps do not cover the whole lateral cylinder surface, but only the part in correspondence of the sensors. Moreover, the clamps effects on the cylinder are different: the one on which is leaned the press compresses the cylinder, the other is a sort of constraint that fixes it

during compression. These two peculiarities make the radial compression asymmetric and hardly interpretable, as in the case of circular sensor Fig. 3.6.

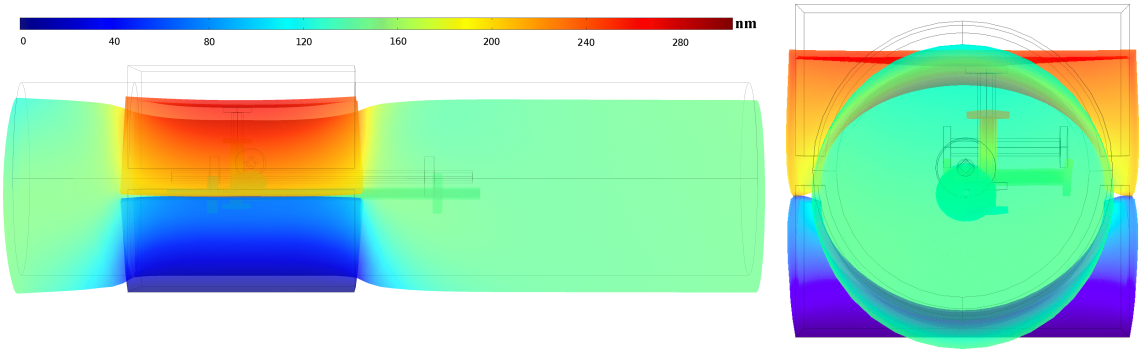

(a) yz view (b) xy view

Figure 3.12: Simulation of radial compression, colors represent the displacement of the objects respect their initial position

Fig. 3.12 are realized by finite element simulation of radial compression; in this figure it is easily visible these differences just described. These differences and the risk to break the concrete compressing it in this way (the uncompressed portion of cylinder is very weak in the region near the compression), lead us to decide to avoid this kind of test.
The only stress test that we have done is vertical compression. Also in this case, due to the presence of rings and cable on the top of cylinder (see Fig. 3.9), we can not compress it directly. To do this without damage rings and cables, we have put on the cylinder top a smaller one made of aluminium ($r = 3$ [cm] $h = 10$ [cm]). In this case the surface uncovered, is smaller than the previous one and does not entail breaking risks. A setback using this cylinder could be that it absorbing a part of compression force generated by the press. This does not allow us to know exactly the force acting on the concrete cylinder. Nevertheless, thanks to the reduced dimension of aluminium cylinder and finite element simulation data, we can neglect this inconvenience. In Fig. 3.13 and Fig. 3.14 are shown the differences between the simulated strains of sensors during the compression of concrete with and without the aluminium cylinder. Except for y sensor there are no differences between to use or not to use the aluminium cylinder. The ostensible problem with y sensor will be easily solved later, when we will discuss about the lateral behaviour of concrete cylinder under compression.
Once we have established that the compressions, with or without the aluminium cylinder, are equal we have started the tests. We have made two series of pressure tests, each series consist of four steps of compression: $0 \div 5$, $0 \div 10$, $0 \div 15$, $0 \div 20$ [kN]. During each compression, the computer that controls the press saves a hundred values of strength. Due to the different acquisition rate, SmartScan saves about a thousand data for each of those of the computer. In order to have the same number of data, during the post analysis phase we have split the wavelength data in hundred consequential clusters, and averaged them. At the same time, we have converted the force value of press into pressure and then in strain using Eq. 3.6. As we expected, z sensor has a negative wavelength shift under pressure along its axis. Fig. 3.15 is only an example, all graphics of all measurements are in App. B. In all plots of sensors wavelength shift vs strain, we can see that the sensors response to the compression is not totally linear, especially for the horizontal sensors Fig. 3.16. In all of these cases data present an undulating behaviour around the general linear trend. Even if

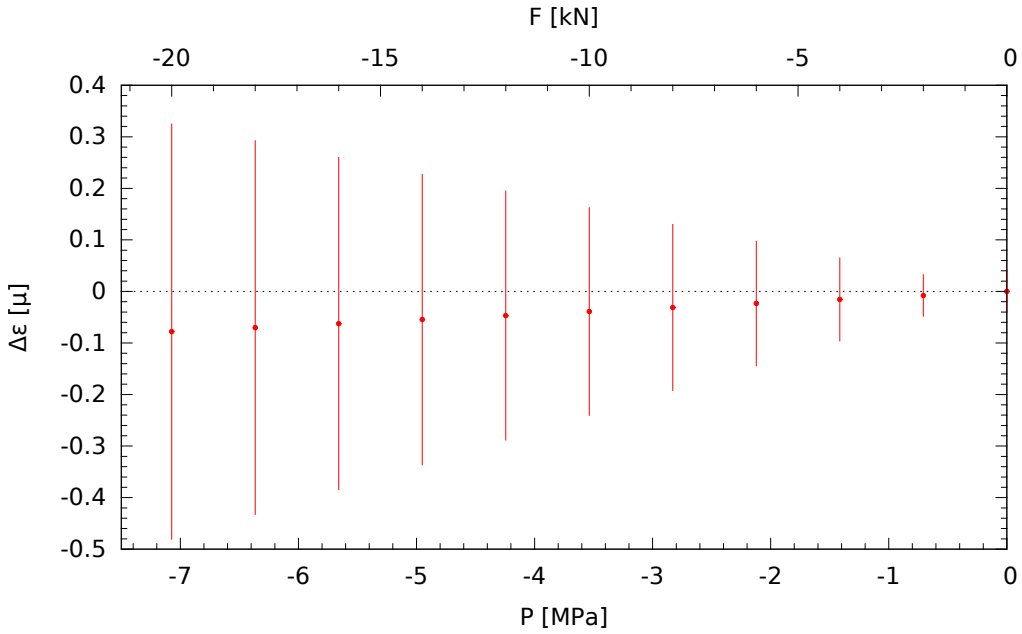

Figure 3.13: Difference between simulated strains of z sensor.

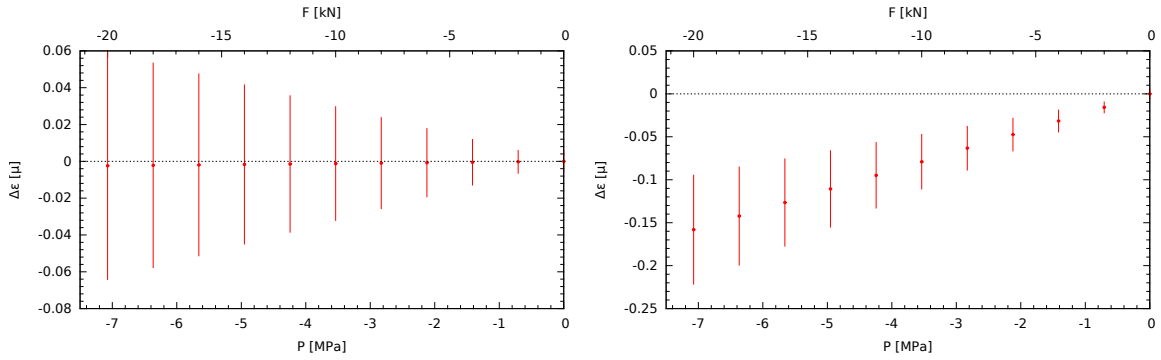

(a) x sensor

(b) y sensor

Figure 3.14: Difference between simulated strains of horizontal sensors

this is apparently in contrast with Eq. 3.4, we imagined similar results. Same measurements previously done on 20 degree sensor have shown a similar relation. This behaviour can be explained considering that our cylinder is not a perfect homogeneous concrete cylinder. Wavelength shift depends directly on the strain and this one depends on the compression, but Eq. 3.6 works only for homogeneous materials. To evaluate exactly the tensors of stress and strain for inhomogeneous elements we should know the kind of imperfection of our element and where they are located. By 3D numerical simulation W.C. Zhu *et al.* [45] have shown how different failures formation inside a concrete cylinder can condition its lateral deformation under vertical compression. These unpredictable lateral deformation affects, in particular, our horizontal sensor elongation or contraction, this produces the behaviour shown in Fig. 3.15 and Fig. 3.16. However, these event does not condition so much the linear trend, then we chose to fit all of plots of wavelength shift of vs strain with a straight line

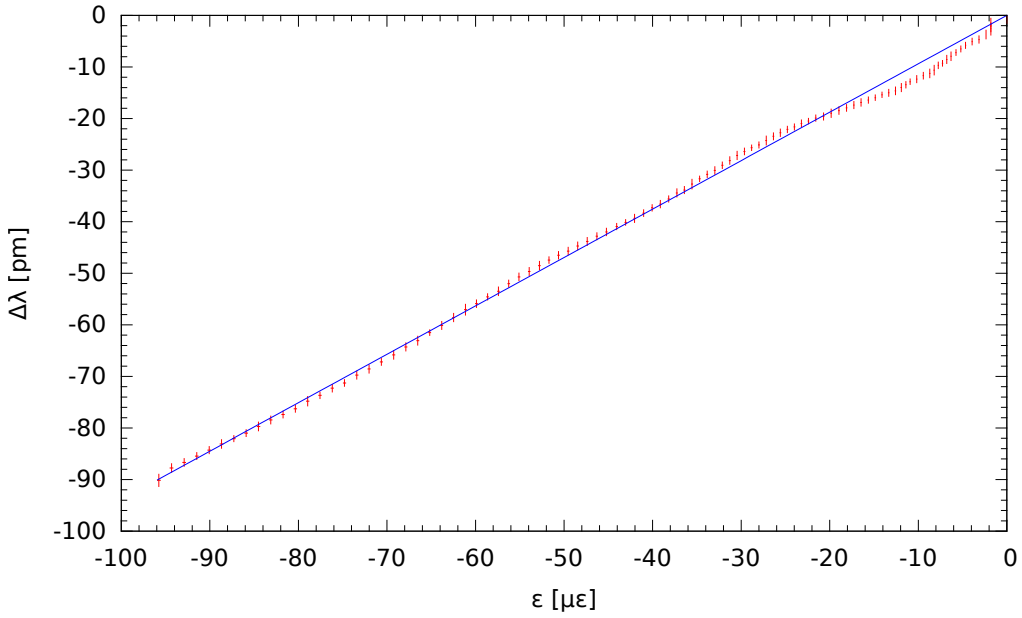

Figure 3.15: Wavelength shift vs strain of z sensor.

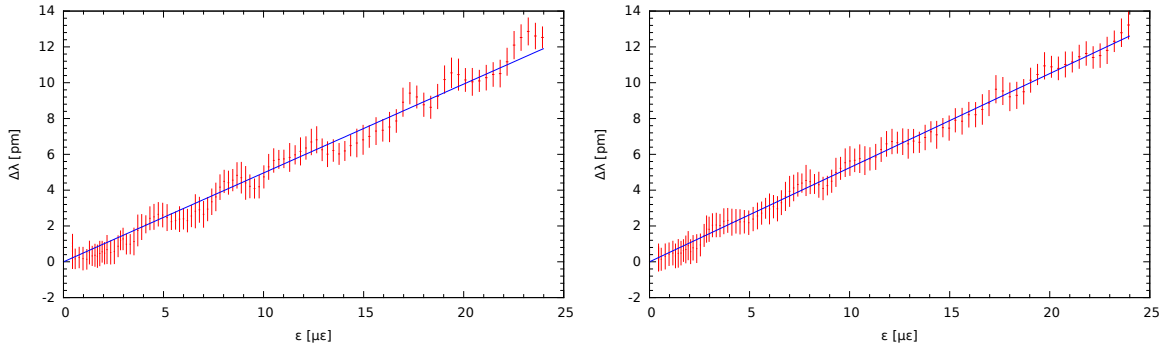

(a) x sensor (b) y sensor

Figure 3.16: Wavelength shift vs strain of orizontal sensors.

like[3] $\Delta\lambda(\varepsilon) = C_\varepsilon \varepsilon$. In Tab. 3.2 are reported all values of data fits.
We have also tried to measure the vertical compression of cylinder during pressure test using a touch-trigger probe, in order to have a direct measurement of vertical strain. Unfortunately, due to the insufficient space to place the touch-trigger probe, we could not do it. Searching in literature about works that use embedded FBGs inside concrete for strain measurement, we discover that in some cases [10, 46] is used the conversion value of bare fiber without correction. In other cases, this problem is solved testing the embedded sensor with specific press able to evaluate the applied strain [8]. The only thing that we could say about C_ε is that the value of 1.2 $[\mathrm{pm}/\mu\varepsilon]$ is an upper bound. All kind of protection that cover the bare fiber absorbs a part of compression or traction applied to the sensor, so for each micro-strain we see a wavelength shift lower than 1.2 [pm].
In our case the best measurement of C_ε is the one of z sensor. The unpredictable lateral

[3] we have imposed that without strain there is not wavelength shift

	z sensor		x sensor		y sensor	
Force [KN]	C_ε [pm/$\mu\varepsilon$]	ΔC_ε [pm/$\mu\varepsilon$]	C_ε [pm/$\mu\varepsilon$]	ΔC_ε [pm/$\mu\varepsilon$]	C_ε [pm/$\mu\varepsilon$]	ΔC_ε [pm/$\mu\varepsilon$]
$0 \div 5$	1.09	0.01	0.34	0.01	0.64	0.01
	0.826	0.007	0.54	0.02	0.67	0.01
$0 \div 10$	0.893	0.005	0.338	0.009	0.505	0.005
	0.956	0.007	0.475	0.007	0.284	0.006
$0 \div 15$	0.747	0.003	0.435	0.006	0.471	0.007
	0.947	0.002	0.44	0.01	0.660	0.005
$0 \div 20$	<u>0.939</u>	<u>0.003</u>	<u>0.496</u>	<u>0.004</u>	<u>0.525</u>	<u>0.002</u>
	1.022	0.003	0.338	0.006	0.416	0.006
	Average	St. Dev.	Average	St. Dev.	Average	St. Dev.
	0.9	0.1	0.43	0.08	0.5	0.1

Table 3.2: Values of angular coefficients (C_ε) of fits and their errors (ΔC_ε). Underlined values are those of Fig. 3.15 and Fig. 3.16, plots of the other are in App. B and App. C

behaviours of cylinder under pressure make the measurements of conversion factors of horizontal sensors unreliable. Furthermore, the impossibility of doing radial compression tests prevents us to have a direct measurement of these factors. Following these considerations, according to the guidelines of previous cited articles and the discussion about the lateral behaviour of cylinder under compression, we have chosen to use the value of $C_\varepsilon = 0.9 \pm 0.1$ [pm/$\mu\varepsilon$] for all three sensors.

CHAPTER 4

Building of interrogation system

In this chapter we are going to show how and what elements we have used to build up the sensors interrogation system. We have realized an instrument with the same function of **SmartScan** finalized to long term measurements in hostile environment. During the system realization we have considered that it will work unmanned for a long time, so we have to match low power consumption and low data amount. This issue has been already faced by the members of *Osservatorio Vesuviano* [47]. They well know the difficulties of working in hostile places, like volcanic or submarine zones. Existent commercial instruments of data acquisitions are principally projected to work in a laboratory. Therefore, the *O.V.* members decided to project and realize an acquisition system specific for measurements in volcanic environments called **Geophysical Instruments for Low power Data Acquisition** (**GILDA**). This datalogger is made by four boards with different function controlled and powered by a fifth main board. The four boards are

- 4 channels ADC (Analog to Digital Converter), to acquire signals from -10 to 10 [V]
- MCU (Micro Controller Unit) with a RS232 port to device communication and control functions
- PLL (Phase Looking Loop) to correlate time with the UTC time
- GPS to get temporal informations

The modular architecture is an important feature that allow user to fix eventually damage, substituting the board and, eventually, add other component. Moreover, this type of architecture reduces the production costs and the power consumption, to $\sim$ 850 [mW]. Due to the needing of a system with eight input channels, we choose to use two ADC boards instead of one.
The inputs for GILDA datalogger must be voltage signals so we must convert the wavelengths into volts. To do this we used a technique based on the discrimination in wavelength between two adjacent channels of an Arrayed Waveguide Gratings (AWG) [49]. The device is composed by a Super Luminescent Diode (SLD), circulator, 1x3 splitter, AWG and six photodiodes. These devices are assembled as Fig. 4.1 shown. The chosen SLD is the **SLD1005S** produced by *THORLABS Inc.* It is mounted on a thermal-controller that keeps its temperature constant. From SLD light goes to the circulator that sends the beam to the 1x3 splitter which divides the input beam into three equal ones and sends them to the FBGs. Once the reflected part of input beam by FBGs comes back to the 1x3 splitter, it works backwards re-combining them into a single beam. This beam comes back to circulator that sends it to

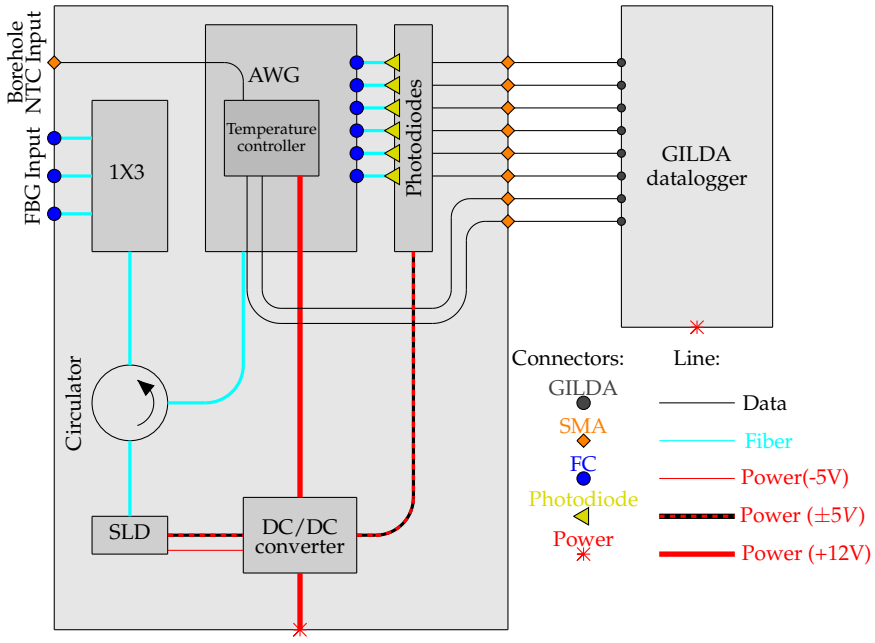

Figure 4.1: Scheme of interrogation system

the AWG. The AWG splits the signal into six beams depending on the wavelength. Each of these split beams is directed to a photodiode that convert it into a signal detectable by GILDA datalogger. The temperature controller on the AWG is divided in two section: one controls and keeps stable the AWG temperature; the other monitors the NTC inside borehole and the one inside the box in which we put the interrogation system. This last one part also connect the two NTC with the datalogger.

4.1 AWG and Photodiodes

The main part of our system is the combination of AWG and photodiodes. As previously said, the FBG generates a small wavelength shift and we expect a shifts whose magnitude is of a pico-meter against wavelength of the order of 10^3 [nm]. To allow to detect these shifts we must empathise it during the acquisition phase. The AWG, photodiodes and a particular way of combine acquired data by datalogger, described later, have been thought exactly to do this.

4.1.1 AWG description

The AWG is a wavelength demultiplexer able to separate the input beam into several ones, depending on wavelength interval. It working principle is based on the interference. The input beam goes into the curved concentric waveguides (see Fig. 4.2) and the different curvature radii generate a phase difference of

$$\Delta\phi_{ij} = \beta\psi(\mathrm{R}_i - \mathrm{R}_j) \tag{4.1}$$

where β is the propagation constant of waveguides, ψ R_i and R_j are whose of Fig. 4.2. In the example of Fig. 4.2 the waveguides are equidistant, but the Eq. 4.1 works also even if they

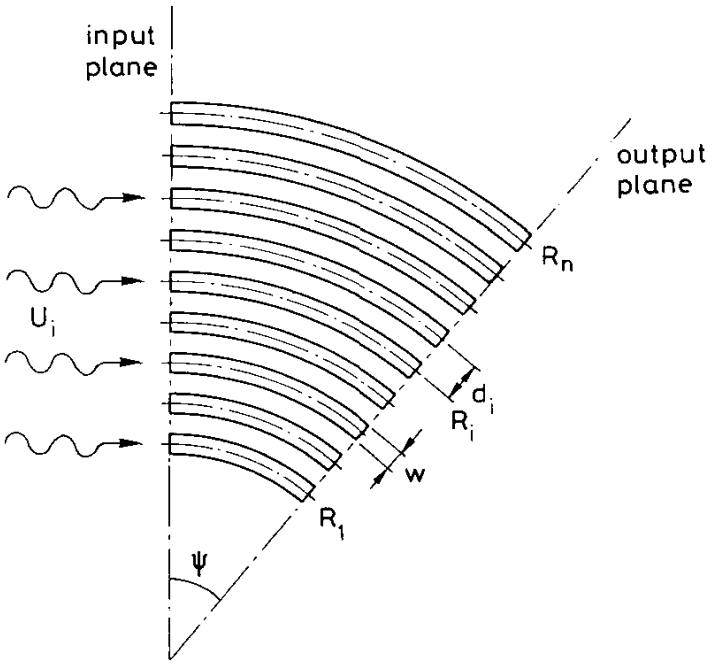

Figure 4.2: Picture number 1 of Smit paper [48]. A scheme of curved waveguides that compose the AWG. U_i is the incident beam, ψ and R_i are the angle and curvature radius, d_i the distance between two consecutive radii and w the waveguide width.

are not. Whereas the phase difference generates interference peaks at different wavelengths, placing the output channels of the AWG in correspondence to the these maximums we get the signal division.
The used AWG is the **1DW-DM1161-02A** produced by **O-Net Communications**. It has 16 channels from 32 to 47 in terms of ITU enumeration, in terms of wavelength from 1539.77 (CH47) to 1551,72 (CH32) [nm]. Each channel is separated from the previous one by 0.8 [nm] and has a FWHM of 0.6 [nm]. An important feature that we have to take under control is that the central wavelength of each channels depend on the temperature. The thermal expansion of AWG waveguides (see Fig. 4.2) changes the value of the curvature radius and, consequently, also the value of the wavelength of the interference peaks. A shift of 1 [°C] causes a global shift of wavelength channels about 2 [pm]. Differently by the concrete cylinder, the AWG will be placed near the surface where the daily and annual temperature shift are about 10 [°C] and 25 [°C] respectively. Due to the expected magnitude of wavelength shift caused by the FBG, to ensure that external temperature variations do not affect AWG working we must fix its temperature with a precision better than 0.1 [°C]. To do this, we have realised an isolating container with an internal fixed temperature of 31 [°C]. This termostatation is achieved using a PT100, which is Resistance Temperature Detectors (RTDs). We have installed it in a feedback circuit with a silicon heater mat in order to use this one to warm up the AWG and the PT100 to control that the temperature is fixed to the established value. This thermostatation system has been tested in laboratory to verify its stability. As Fig. 4.4 shows our system keeps the temperature constant within an interval of 0.03[°C].

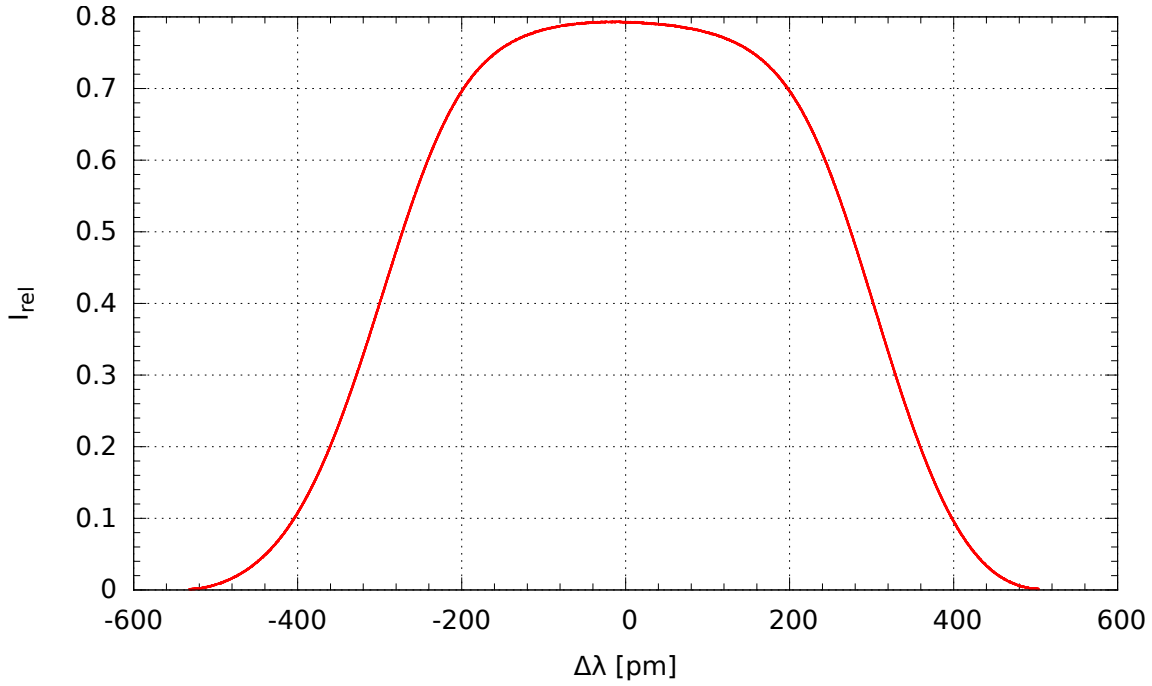

Figure 4.3: Example of an AWG channel. On y axis the intensity of signal exiting from AWG against the incoming one. On x axis the wavelength shift with respect to the central channel wavelength.

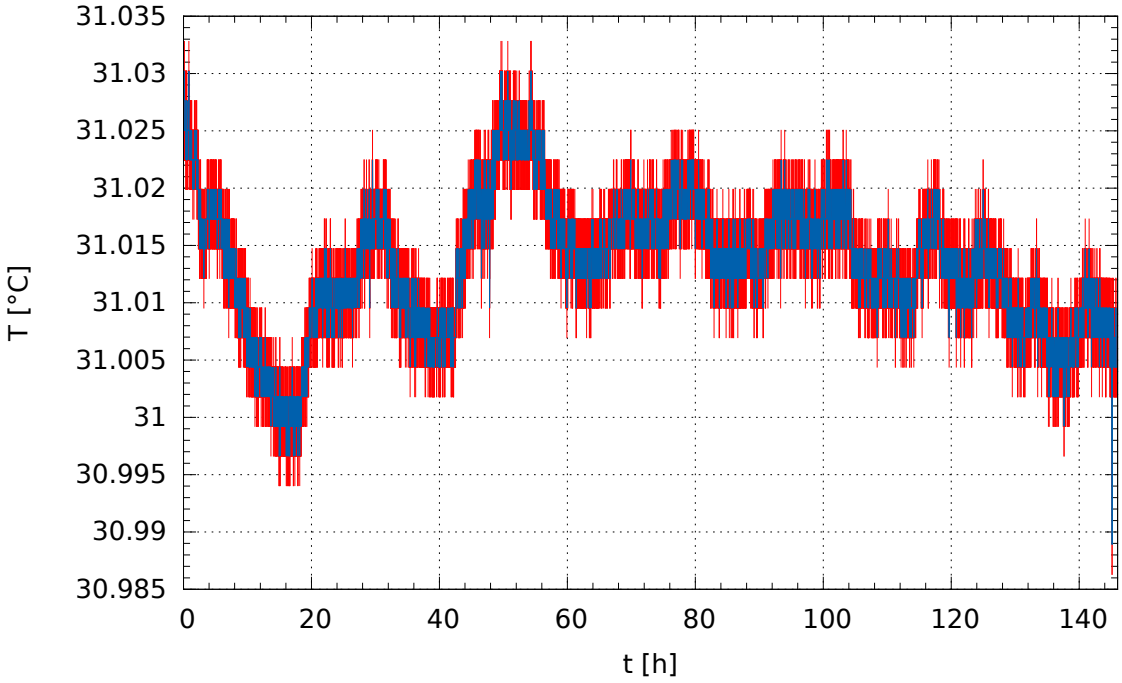

Figure 4.4: Behaviour of the temperature inside the thermostat during six days against external temperature shift of 5 [°C], blu points represent the data while red one are the asccociated uncertainties.

4.1.2 Photodiodes

The photodiodes used are the **InGaAs PIN photodiodes** produced by Hamamatsu Photonics K. K. Their spectral response range goes from 900 to 1700 [nm] with an intensity peak at 1550 [nm]. Two important features of these devices are: the low dark current of about 20 [pA], and the low Noise Equivalent Power (NEP) of about $3 \cdot 10^{-15}$ [W/$\sqrt{\text{Hz}}$]. This kind of photodiodes is realized to work with wavelengths around $1300 \div 1550$ [nm] and hence agrees with our FBGs that have central wavelengths of 1544, 1547 and 1549 [nm]. Due to the combination of FBG and AWG, as we will explain later, the light intensity on photodiodes is very low. Consequently, also the current generated by photodiodes is low (about 100 [nA]). In order to better detect it, we choose to install the photodiode on a transimpedance amplifier mode with a low-pass filter and an inverting amplifier (Fig. 4.5). The first amplification

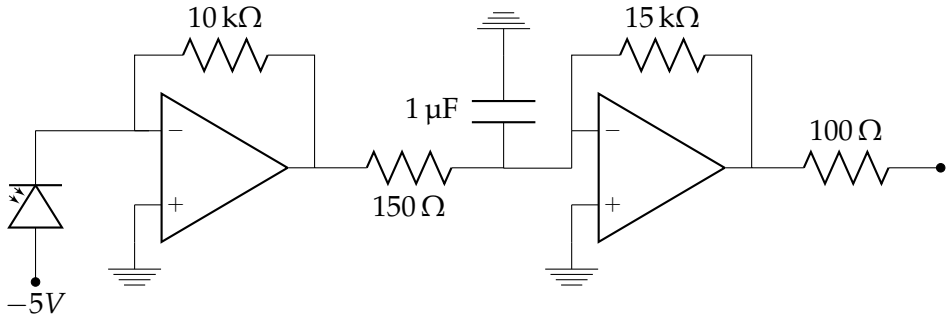

Figure 4.5: Scheme of used amplifer

stage converts photodiode current into volts, amplifying it by a factor of 10^4, the second stage gives an additional amplification of 100. Overall, starting from a current about 100 [nA], we have a magnitude of voltage difference up to 1 [V]. The capacitor is installed to filter eventual high frequency noise, due to power system or circuit elements.
The low-pass filter, formed by capacitor and the resistor of 150 [Ω], does not affect our measurement. Its cut off frequency is about 1 [kHz], while we expect that our strain data will show a significative change with a frequency lower than 1 [Hz].

All of the devices which have been shown in Fig. 4.1, have been assembled in an aluminium box. In the final set-up shown in Fig. 4.6 we have mounted seven photodiodes instead of six. The seventh photodiode has been added to control the trend of photodiodes background noise.

4.2 Power Ratio

The responsivity of photodiode, Fig. 4.7, shows that within a range of 50 [nm] around the responsivity peak (1550 [nm]) there are no differences in photodiode response. Since we work exactly in this wavelength range, using only a photodiode for each channels does not allow us to detect wavelength variations. To be able to do this we choose to use the system developed by H. Su and X. Guang Huang [49]. Their technique is based on using two photodiodes for each FBG, illuminating them by splitting signal coming from FBG with the AWG. Their AWG is chosen in order to have the central wavelengths of FBGs in the

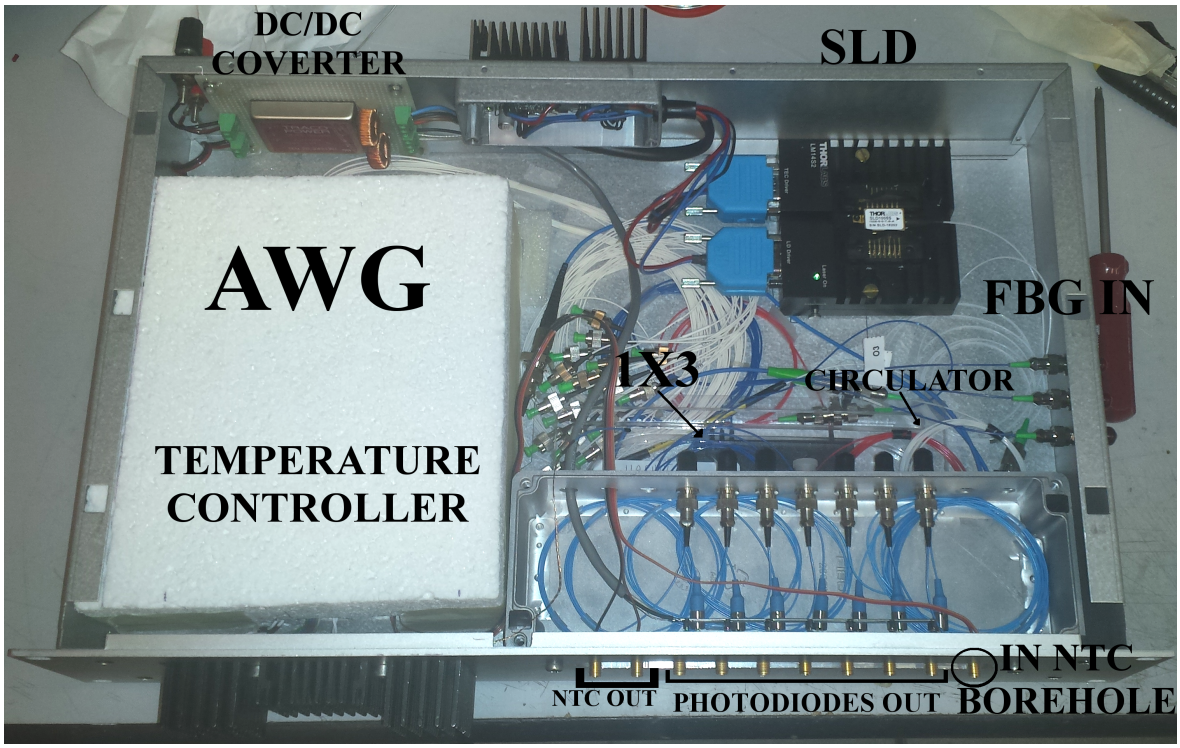

Figure 4.6: Final set-up of interrogation system.

middle between two AWG channels, as Fig. 4.8 shown. The light power detected by the two photodiodes connected to two sequential AWG channels can be evaluated as

$$P_n(\lambda_B) = (1-L)\int_0^{+\infty} I_s(\lambda) R_{FBG}(\lambda,\lambda_B) T_{n,AWG}(\lambda) d\lambda \tag{4.2a}$$

$$P_{n+1}(\lambda_B) = (1-L)\int_0^{+\infty} I_s(\lambda) R_{FBG}(\lambda,\lambda_B) T_{n+1,AWG}(\lambda) d\lambda \tag{4.2b}$$

where n is the channel number, L is attenuation factor of system, $I_s(\lambda)$ is the light source intensity[1],λ_B is the central wavelength of FBG, $R_{FBG}(\lambda,\lambda_B)$ is the reflection function of FBG and $T_{n,AWG}(\lambda)$ the transmission function of n-th AWG channel. The voltage measured by datalogger is

$$V_n(\lambda_B) = V_s P_n(\lambda_B) \tag{4.3}$$

where V_s is the conversion coefficient that includes the effects of photodiode and amplification circuit[2]. The values of each P_n, and so V, depend only by λ_B. The choice of AWG has been made in order to have the central wavelength of FBG in the middle of two channels. In this way,if the FBG reflected signal is in this position, a wavelength shift causes an opposite behaviour in the signals intensity exiting from AWG channels. Indeed, as we can see in Fig. 4.8, an increase of λ_B increases the product between R_{FBG} and $T_{n+1,AWG}$ and hence the intensity of signal exiting from $n+1$ channel, at the same time this decreases the signal exiting from channel n. To capitalise on this behaviour, they combine the couple of signal

[1] In our case, in the range of ~ 0.1 [nm] of wavelength shift we can assume $I_s(\lambda)$ constant

[2] As it is possible to see in Fig. 4.7, we can assume V_s as constant since we work in the wavelength range in which the photodiode has a constant response

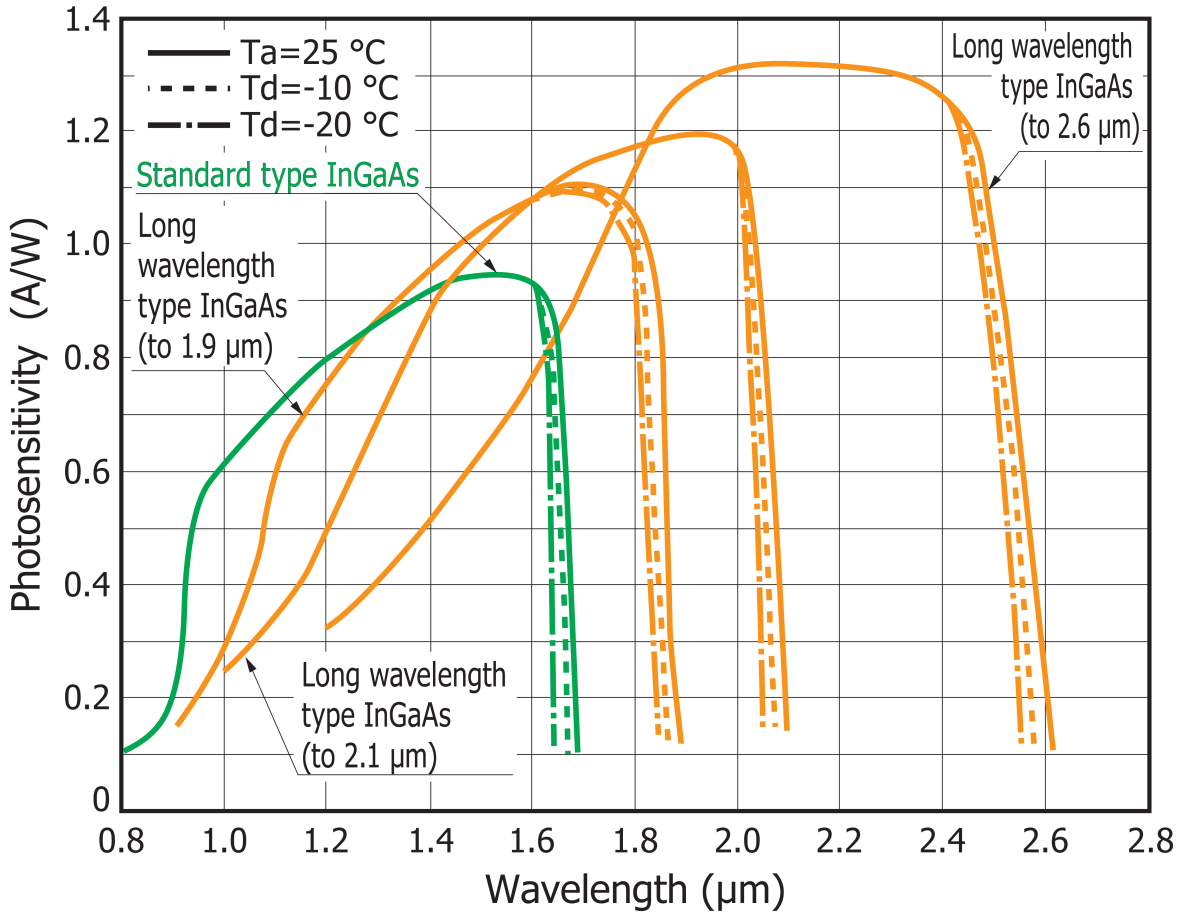

Figure 4.7: Graphic realized by Hamamatsu Photonics K. K. about their InGaAs photodiodes responsivity. Our photodiode is a standard one, whose curve is the green one.

coming from the same FBG in the following way

$$S(\lambda_B) = \frac{V_{n+1}(\lambda_B) - V_n(\lambda_B)}{V_{n+1}(\lambda_B) + V_n(\lambda_B)} \tag{4.4}$$

The S function (Eq. 4.4) is called *power ratio*. Due to how S is defined, all constant parameters does not affect its value. Simplifying all of these we can rewrite Eq. 4.4 as

$$S(\lambda_B) = \frac{\int_0^{+\infty} \left(R_{FBG}(\lambda, \lambda_B) T_{n+1,AWG}(\lambda) - R_{FBG}(\lambda, \lambda_B) T_{n,AWG}(\lambda)\right) d\lambda}{\int_0^{+\infty} \left(R_{FBG}(\lambda, \lambda_B) T_{n+1,AWG}(\lambda) + R_{FBG}(\lambda, \lambda_B) T_{n,AWG}(\lambda)\right) d\lambda} \tag{4.5}$$

It is clear from Eq. 4.5 and Fig. 4.8 that the values of S depend on the integral of the product between FBG reflection function and the AWG transmission one. All of elements that compose S are positive, so its sign is determinate only by its numerator. When λ_B is in the middle of the two AWG channels $S = 0$. A negative wavelength shift makes S negative, vice versa with positive wavelength shift. The denominator of S makes its value restricted to the interval of ± 1. Indeed, once the shift is as high as the FBG function is out from one of the two channels, the product with it becomes approximately 0, and the ratio simplifies itself to ± 1.
Su and Guang Huang tested their method warming up an FBG in a box, which can control

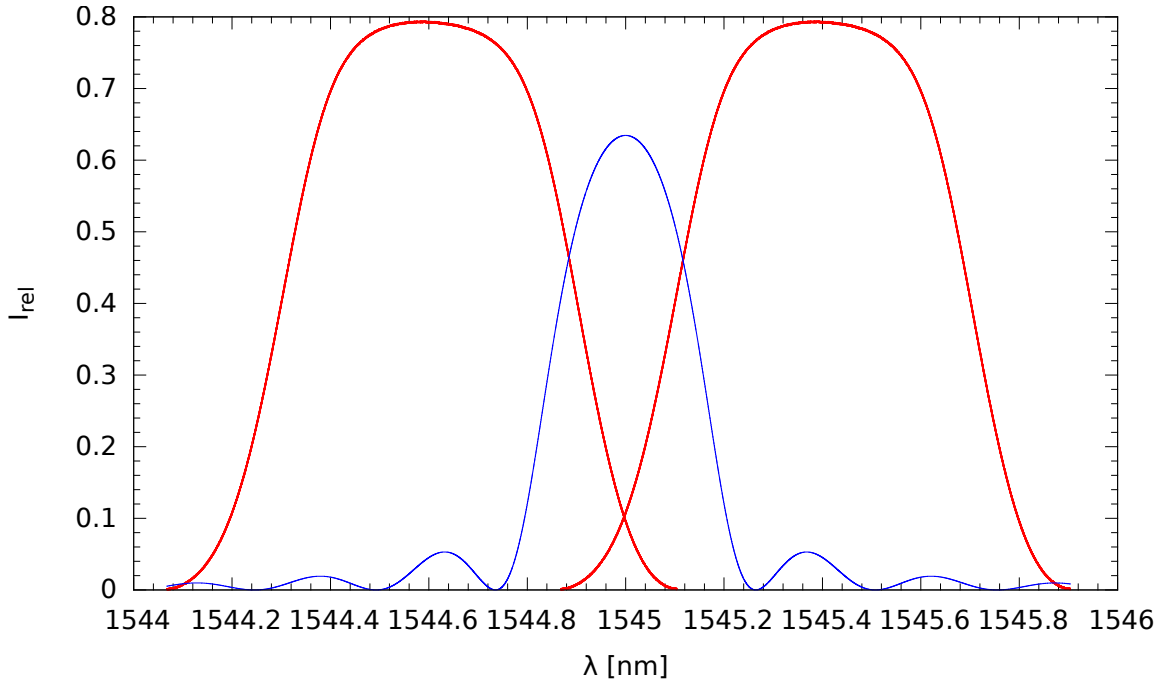

Figure 4.8: Example of an FBG reflection function (R_{FBG}) with central wavelength of 1545 [nm] and the two AWG channels transmission ($T_{n,AWG}$ on left, $T_{n+1,AWG}$ on right) functions used with the Su and Guang Huang method [49].

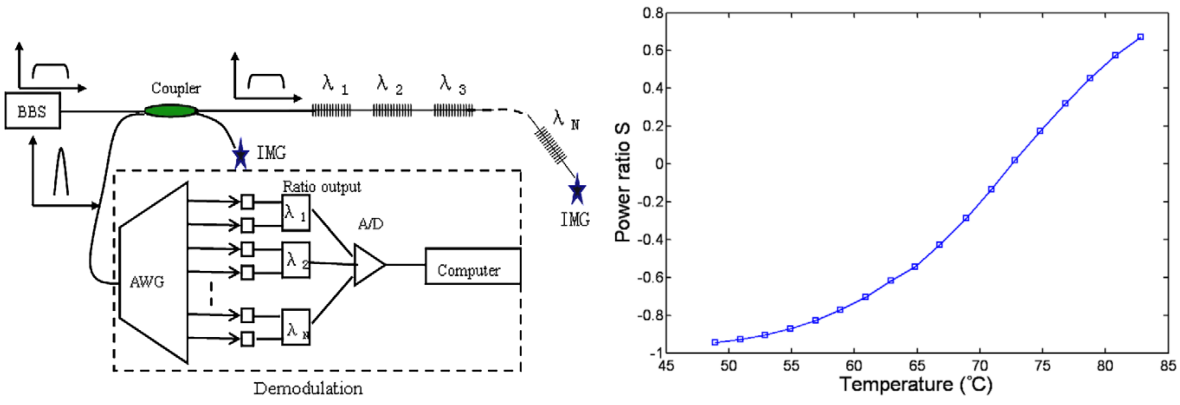

(a) Experimental set up

(b) Experimental data S vs temperature

Figure 4.9: Figures 1 and 6b of Su and Guang Huang paper [49].

temperature within ± 0.2 [°C]. Their results (Fig. 4.9b) show that within an interval of ± 0.5 around the zero of S, it is linear with respect to temperature variation and, due to the relation between temperature and wavelength, also with respect to wavelength shift. In term of degrees this linearity interval is about 15 [°C], that corresponds to a wavelength shift from the middle point of two AWG channels of about ± 1001 [pm],.

To verify the applicability of this technique with our instrument, it should be tested with the final set up of interrogation system. Unfortunately, we do not have the GILDA datalogger yet. So, to test the AWG and photodiodes, we have used the SmartScan to measure the wavelengths and a multimeter and the NI USB-6251 BNC, a DAQ module of *National*

Instruments, to measure volts values. During these tests we have not used the FBGs inside the concrete cylinder. We don't need to use exactly these FBG we can choose just one which is able to have a wavelength shift within an interval of some tens of pico-meters, centred in the middle of two AWG channels. Moreover, not to use the FBGs inside the concrete has simplified the tests. To generate wavelength shift with these sensors we can only compress or warm up the cylinder and in Ch. 3 we have explained how these processes are hardly controllable. The sample FBG used was fixed to two blocks, both fixed to the optical bench. One of these has a slide controlled by a micro-metric screw, that allows movements along the FBG axis (Fig. 4.10). The other, in correspondence to the glueing point of fiber, has a piezo-electric that, controlled by a wave-generator, stretches and compresses the fiber. The fiber with FBG, SmartScan and AWG are connected through a circulator. These tests have been

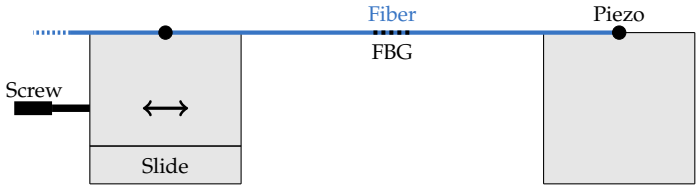

Figure 4.10: Schematization of used system to stretch the fiber

made in two steps, in the first one using the screw we have elongated the FBG of 100 [μm], that in terms of wavelength shift are $\sim$ 0.4 [nm]. In this way we have acquired several values of S, in order to find the position of its zero in terms of screw move. The second steps has been to place the FBG in the position of zero of S and activate the piezoelectric with a triangular wave 20 [s] periodic. The continuous and repetitive movements of piezoelectric allow us to analyse better the linear zone of S. In the first case the volts values are acquired using the multimeter, in the second one with the NI device. During the measurements of the first step, we have noted that, due to the little dimension of gluing point between fiber and blocks, the fiber elasticity acting like a "spring". Once the fiber is put in traction, it starts to swing impeding the stability of reflected wavelength. Another source of uncertainty for this measure was the simultaneous use of SmartScan and our interrogation system. The peaks of intensity generated by the laser inside SmartScan and detected by the photodiodes contribute to the instability of measurement. For these reasons, the uncertainties of wavelengths and volts are higher then those that we will have once the system will be installed. Indeed, in this case the sensors fibers walled up into the concrete are totally glued to the steel protection. Also in the second step we do not have effects like these, the continuous movements of piezoelectric does not let to the fiber elasticity enough time to relax it.
The results of first step of measurements are in Fig. 4.11 and Tab. 4.1.
In the second step we have measured the time evolution of wavelength and volts separately to avoid eventual interferences between the SmartScan internal light source and the AWG. In order to avoid noise, we have filtered volts signals with a RC-filter with a cut-off frequency of 1.5 [Hz][3]. Both acquisitions are of 100 [s] and the voltage amplitude that controls the piezoelectric is so that the S varying from -0.6 to 0.6
The results of this measure are in Fig. 4.12 and Fig. 4.13.
The high differences in data uncertainties between Fig. 4.11 and Fig. 4.13 are due to the different way of measuring. In the second step of measurements the "spring" behaviour of fiber

[3]The value of resistor is 22 [kΩ] and capacitor one is 4.7 [μF]

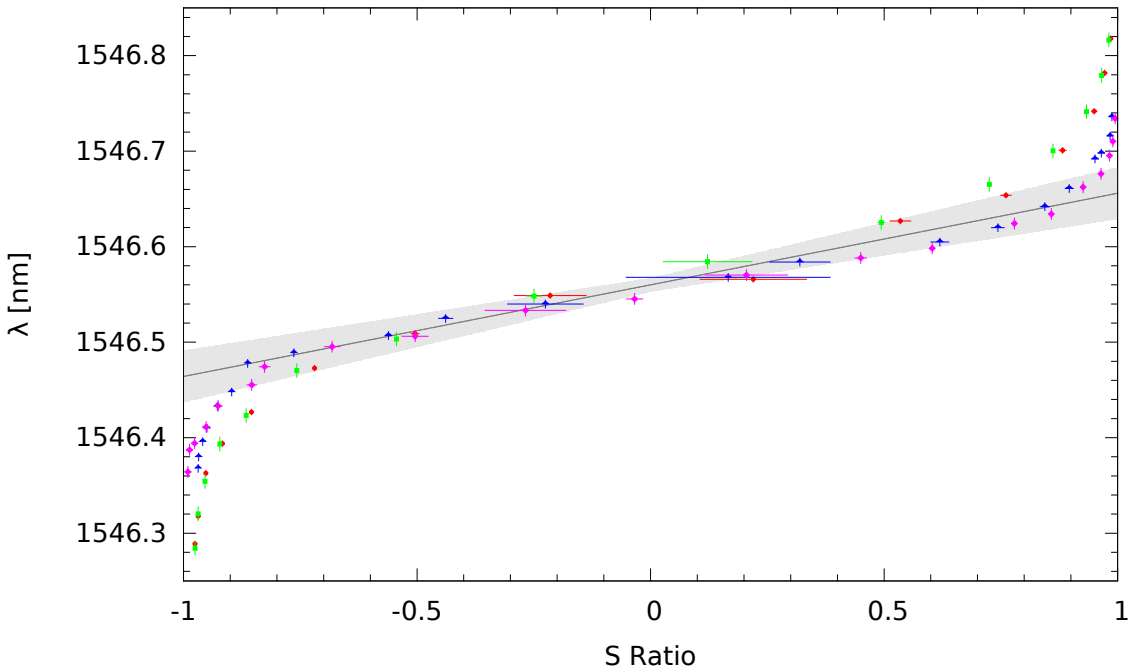

Figure 4.11: First step of measurements. Experimental data of wavelength vs power ratio and average fit. Each color in Fig. 4.11 represents a different series of measurements, every one fitted using the data inside an interval of ± 0.6 around the zero of S.The straight line plotted is the average of all of this fits. All of fit values are in Tab. 4.1

Data series	m [nm]	Δm [nm]	q [nm]	Δq [nm]
red ●	0.10	0.02	1546.562	0.008
green ■	0.115	0.007	1546.570	0.003
blue ▲	0.082	0.005	1546.557	0.002
purple ♦	0.084	0.005	1546.551	0.002
average	0.10	0.02	1546.560	0.008

Table 4.1: Fits of all data series of first step, m and q are the slope and the intercept of stright lines.

is negligible, this kind of effect appears only if we stress the fiber with discrete movements, the continuous movements of piezoelectric solve this problem. While, the problem of noise due to the simultaneous measurements was simply solved measuring with the SmartScan and with the interrogation system in two separate times.

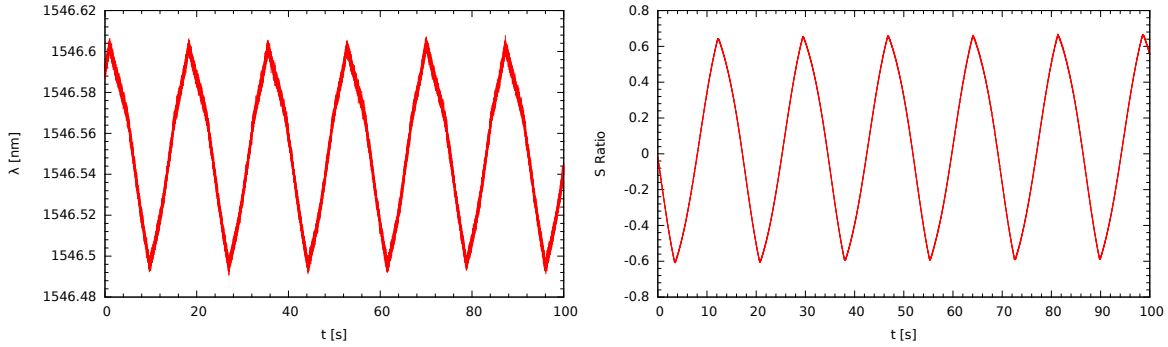

(a) λ vs t (b) S vs t

Figure 4.12: Time evolution of λ and S while piezoelectric is moveing.

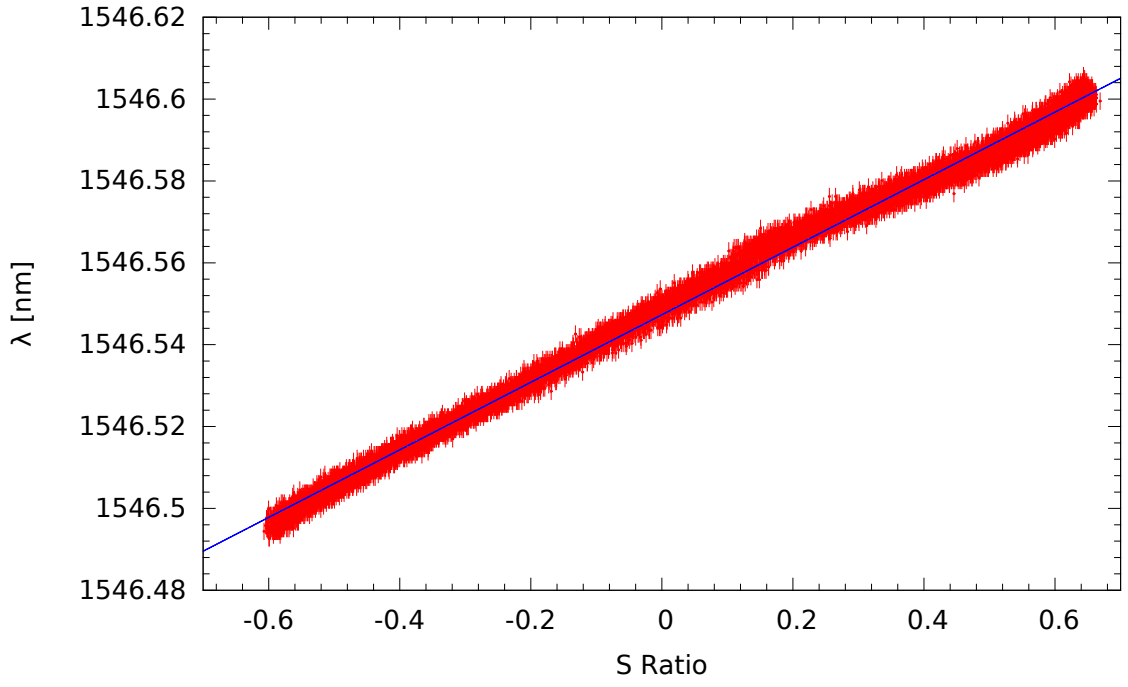

Figure 4.13: Second step of measurements. Experimental data of wavelength vs S and fit. The fitted function is $\lambda(S) = mS + q$ where $m = 0.08251 \pm 5 \cdot 10^{-5}$ [nm] and $q = 1546.54731 \pm 2 \cdot 10^{-5}$ [nm].

CHAPTER 5

Conclusions

In this thesis is shown how we projected, and then realized, a new kind of tri-axial strain gauge for geological measurements based on FBG sensors and the opto-electronic system of interrogation and control.
In Ch. 3 it is illustrated how we have realized and tested the sensor. During these tests we have verified that the relation between strain and wavelength shift is linear within a strain range of $\sim$ 100 $[\mu\varepsilon]$. In the last section of this chapter we have also explained the choice reasons of 0.9 ± 0.1 $[\mathrm{pm}/\mu\varepsilon]$ as conversion factor between strain and wavelength shift for all of three sensor.
In Ch. 4 it is shown the interrogation system and the results of its calibration, which prove that this system, thanks to the low value of RMS noise ($\sim 7 \cdot 10^{-4}$) of S, the function used to convert voltage acquired signals by the datalogger into wavelength shift, is able to measure the wavelength shift with a resolution of 0.1 [pm] and a dynamic range of 120 [pm] ($\pm$60 [pm]). Furthermore, the low power consuming opto-electronic devices used to assemble the interrogation system guarantee a proper and durable operation of the system even if it is powered by battery and solar panels.
In conclusion, matching the results of these two chapters, we see that with our device (sensor and interrogation system) we can measure strains values (in modulus) with an accuracy of $0.1[\mu\varepsilon]$ and a dynamic range of 100 $[\mu\varepsilon]$.

We have planned to install the sensor next spring in order to have as many a possible data before the end of the project, established at the end of 2016.
However, even after the end of MED-SUV, this sensor will work and will monitor the rock in which it is walled up. Continuing the data analysis we can enhance the knowledge about the effect of the volcano activity on the ground near it.

An important aspect of this sensor that we want to underline is that even if it has been projected to be tri-axial this feature only concerns the strain measurements. Using this sensor we can detect the strain along three Cartesian axes, but, as we have seen in Ch. 3, the perturbation that cause rock deformation can not be described only by a tri-axial strain analysis. A compression along an axis deforms an object along all spatial dimensions, that means that the same strain could be caused by different events; without other information we can not discern these events using only the strains. To improve the study of this kind of phenomena, we could match the sensor measurements with other informations as site morphology or data coming from other type of devices, e.g. seismographs. In this way we can better

describe the perturbations that cause the strains measured by sensor. E.g. if we know that the measured strain is caused by a seismic P-wave, then, due to the wave features, the strain magnitude must be higher along the propagation wave direction. Observing the differences between the strains magnitude measured by sensors, we can estimate the propagation wave direction.

In order to better monitor a larger area we can create a network of sensor like this, all controlled by only one interrogator based on device like a Fabry-Pérot tunable filter (a device based on a Fabry-Pérot which cavity has a movable mirror) [50] instead of AWG. This changing in the interrogation system cause an increasing in the uncertainty of final data, but on the other hand this new device can scan wavelength interval of several tens of nano-meter. This feature makes the Fabry-Pérot tunable filter suitable to control tens of FBG based sensor. Another device with the same function of Fabry-Pérot tunable filter is the Reflective-Matched FBG [51]. This device works like the previous one; in this case it is used a FBG on a movable sustaining system to achieve the same effect of the cavity with movable mirror.
Due to the higher uncertainties and costs we have not considered these alternative systems during the designing of our sensor.

APPENDIX A

Solution of circular sensor's equation

As we have said in Sec. 3.4 we have to solve

$$\begin{cases} L_1 = a \int_{\theta}^{\gamma+\theta} \sqrt{1 - e^2 \sin^2(x)} dx \\ L_2 = a \int_{\theta+\frac{\pi}{2}}^{\gamma+\theta+\frac{\pi}{2}} \sqrt{1 - e^2 \sin^2(x)} dx \\ \nu = -\dfrac{\varepsilon_a}{\varepsilon_b} \end{cases} \tag{A.1}$$

The first two integrals are analytically unsolvable. In our case we can avoid this problems by considering:

- $\sin^2(x)$ has as maximum value 1
- $e^2 = 1 - \left(\frac{b}{a}\right)^2$ due to little differences expected between a and b ($\sim 0.005\%$) can be approximated with: $e \simeq 0$

Thanks to this we can approximate the two integrals in this way

$$\int_{\alpha}^{\beta} \sqrt{1 - e^2 \sin^2(x)} dx \simeq \int_{\alpha}^{\beta} \left(1 - \frac{1}{2} e^2 \sin^2(x)\right) dx \tag{A.2}$$

Now it can be easily integrated and solved getting the length of two sensors in function of a and b

$$L_1 = a \left(\gamma - \frac{1}{4} e(a,b)^2 (\gamma - \sin(\gamma+\theta)\cos(\gamma+\theta) + \sin(\theta)\cos(\theta))\right) \tag{A.3a}$$

$$L_2 = a \left(\gamma - \frac{1}{4} e(a,b)^2 (\gamma + \sin(\gamma+\theta)\cos(\gamma+\theta) - \sin(\theta)\cos(\theta))\right) \tag{A.3b}$$

With the third of Eqs. A.1 we can link a to b

$$\nu = -\frac{\varepsilon_a}{\varepsilon_b} = -\frac{a-r}{r}\frac{r}{b-r} = \frac{a-r}{r-b} \tag{A.4}$$

$$b(a) = r - \frac{a-r}{\nu} \tag{A.5}$$

To simplify the solution process, we note that in Eqs. A.3 there is a particular alternation in signs that can help us. Summing and subtracting each other the Eqs. A.3 we get:

$$L_1 + L_2 = -\frac{1}{2}a\gamma\left(e(a)^2 - 4\right) \tag{A.6a}$$

$$L_1 - L_2 = \frac{1}{2}ae(a)^2\sin(\gamma)\cos(\gamma + 2\theta) \tag{A.6b}$$

Eq. A.6a does not depend by θ and so expanding $e(a)$ and γ (that is equal to the ratio between the initial sensor's length L_0 and the circumference's radius) this become an equation with only a as variable.

$$L_1 + L_2 = \frac{L_0\left(a^2\left(3\nu^2+1\right) - 2ar(\nu+1) + r^2(\nu+1)^2\right)}{2ar\nu^2} \tag{A.7}$$

Using that

$$\frac{L_1 + L_2}{L_0} = \left(\frac{L_1}{L_0} - 1\right) + \left(\frac{L_2}{L_0} - 1\right) + 2 = \varepsilon_1 + \varepsilon_2 + 2 \tag{A.8}$$

we can simplify Eq. A.7:

$$\frac{a^2\left(3\nu^2+1\right) - 2ar(\nu+1) + r^2(\nu+1)^2}{2ar\nu^2} - \varepsilon_1 - \varepsilon_2 - 2 = 0 \tag{A.9}$$

Since a, r and ν are different from 0, we can change Eq. A.9 into a simple II grade equation. The solutions of this equation are:

$$a = \frac{r\left(1 + \nu + \nu^2(2 + \varepsilon_1 + \varepsilon_2) \pm \nu\sqrt{(\nu-1)^2 + \nu^2(\varepsilon_1+\varepsilon_2)^2 + 2(\varepsilon_1+\varepsilon_2)(1+\nu+2\nu^2)}\right)}{1+3\nu^2} \tag{A.10}$$

Because of a must be longer than b, the right solution is the one with $-$. Dividing both members of Eq. A.10 by r and subtracting to them 1 on the left side we get the strain of a axis

$$\varepsilon_a = \nu\frac{\nu(\varepsilon_1+\varepsilon_2-1) + 1 - \sqrt{(\nu-1)^2 + \nu^2\left(\varepsilon_1+\varepsilon_2\right)^2 + 2\left(2\nu^2+\nu+1\right)\left(\varepsilon_1+\varepsilon_2\right)}}{1+3\nu^2} \tag{A.11}$$

Using again the third of Eq. A.1, it is easy to evaluate ε_b

$$\varepsilon_b = -\frac{\nu(\varepsilon_1+\varepsilon_2-1) + 1 - \sqrt{(\nu-1)^2 + \nu^2\left(\varepsilon_1+\varepsilon_2\right)^2 + 2\left(2\nu^2+\nu+1\right)\left(\varepsilon_1+\varepsilon_2\right)}}{1+3\nu^2} \tag{A.12}$$

To get the value of θ in function of a ε_1 and ε_2, we expand $e(a)$ in Eq. A.6b and rewrite $L_1 - L_2$ as

$$L_1 - L_2 = L_0\left(\frac{L_1}{L_0} - \frac{L_2}{L_0}\right) = L_0\left(\frac{L_1}{L_0} + 1 - \frac{L_2}{L_0} - 1\right) = L_0\left(\varepsilon_1 - \varepsilon_2\right) \tag{A.13}$$

Taking into account these considerations, we can write

$$\cos(\gamma + 2\theta) = \frac{2aL_0\left(\varepsilon_1 - \varepsilon_2\right)\nu^2}{\sin\left(\gamma\right)\left(\nu+1\right)(a-r)(a(\nu-1)+r(\nu+1))} \tag{A.14}$$

and then

$$\theta = \frac{1}{2}\arccos\left(\frac{2aL_0\left(\varepsilon_1 - \varepsilon_2\right)\nu^2}{\sin\left(\gamma\right)\left(\nu+1\right)(a-r)(a(\nu-1)+r(\nu+1))}\right) - \frac{\gamma}{2} \tag{A.15}$$

APPENDIX B

Plots of wavelength shift vs pressure z sensor

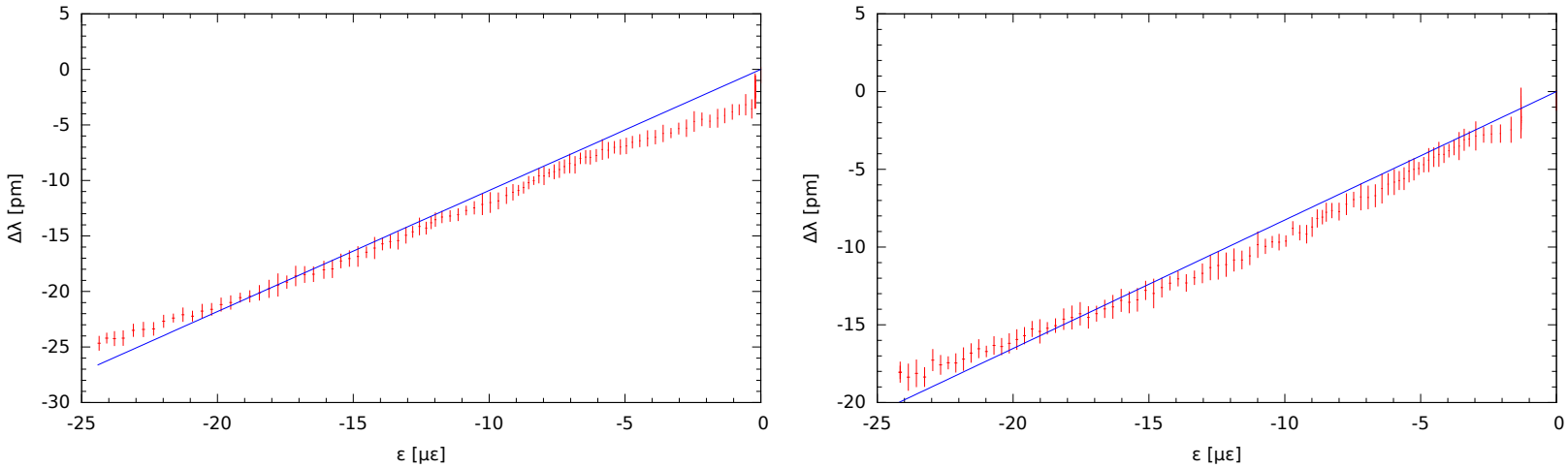

(a) (b)

Figure B.1: 0 ÷ 5 [kN]

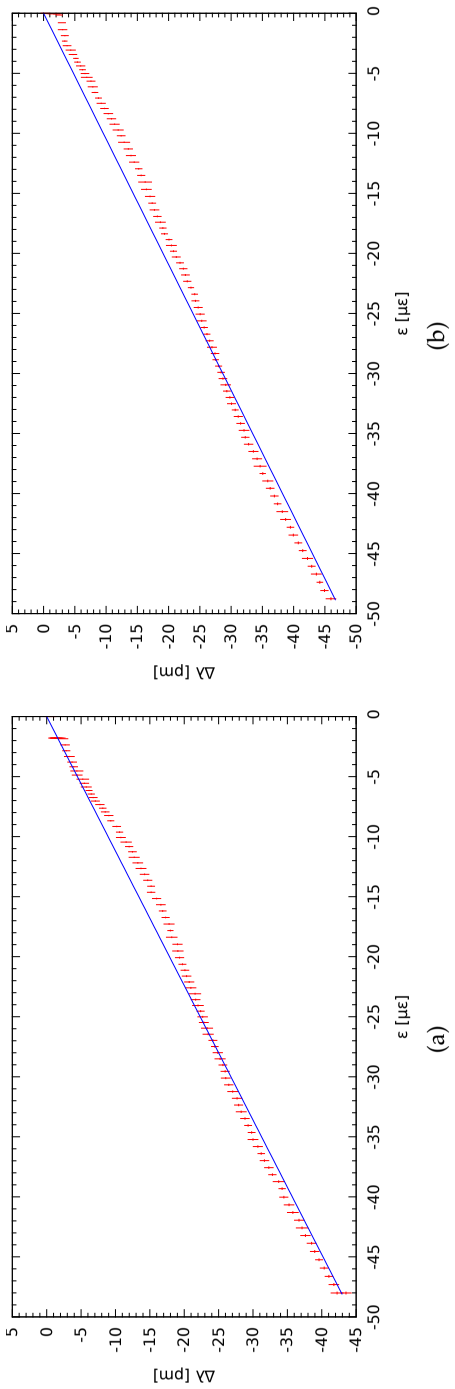

Figure B.2: 0 ÷ 10 [kN]

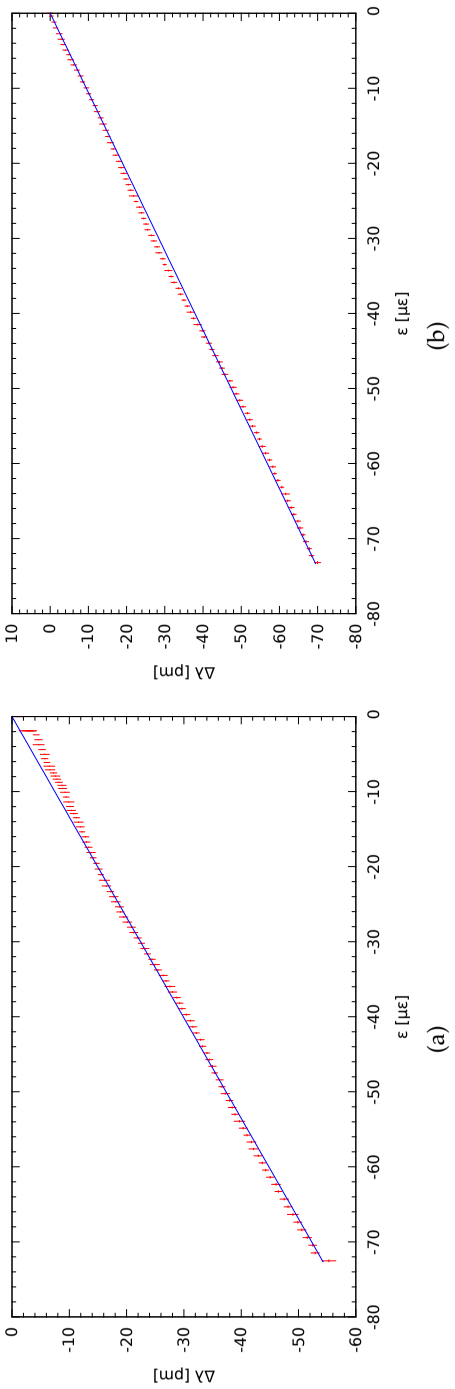

Figure B.3: 0 ÷ 15 [kN]

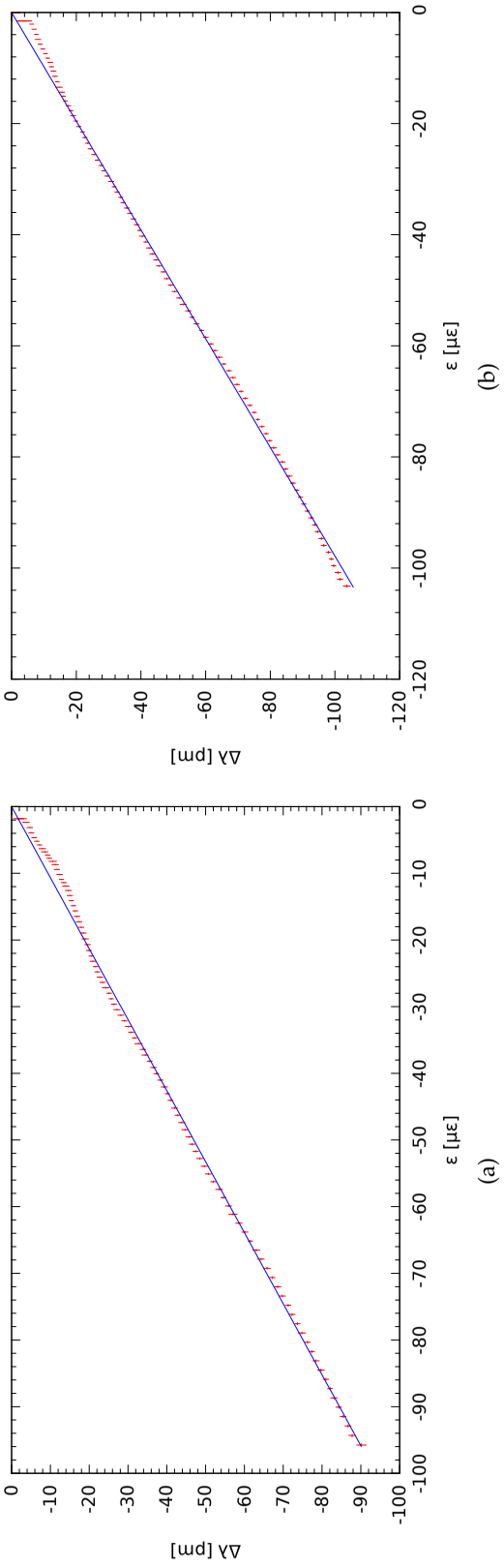

Figure B.4: 0 ÷ 20 [kN]

APPENDIX C

Plots of wavelength shift vs pressure horizontal sensors

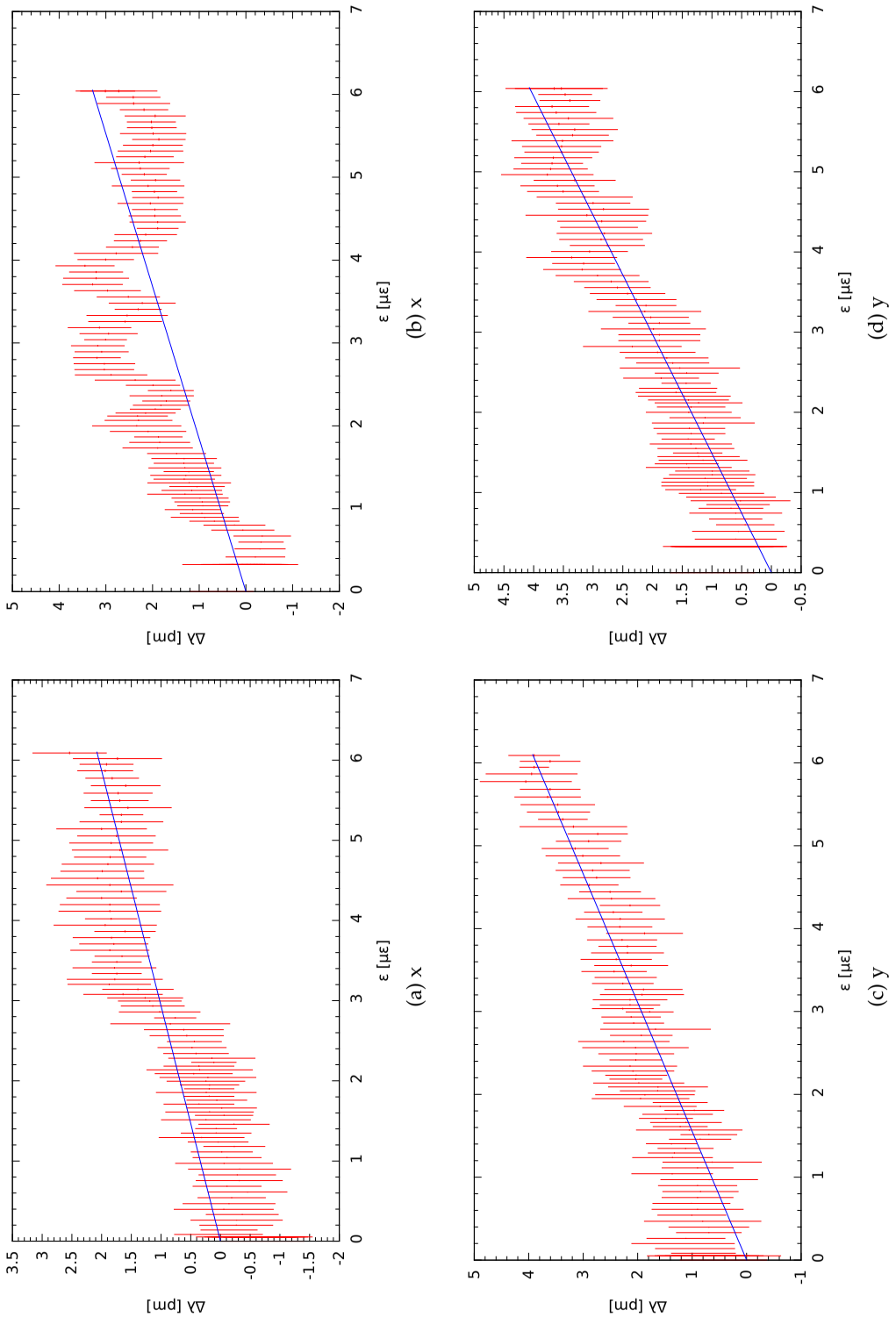

Figure C.1: 0 ÷ 5 [kN]

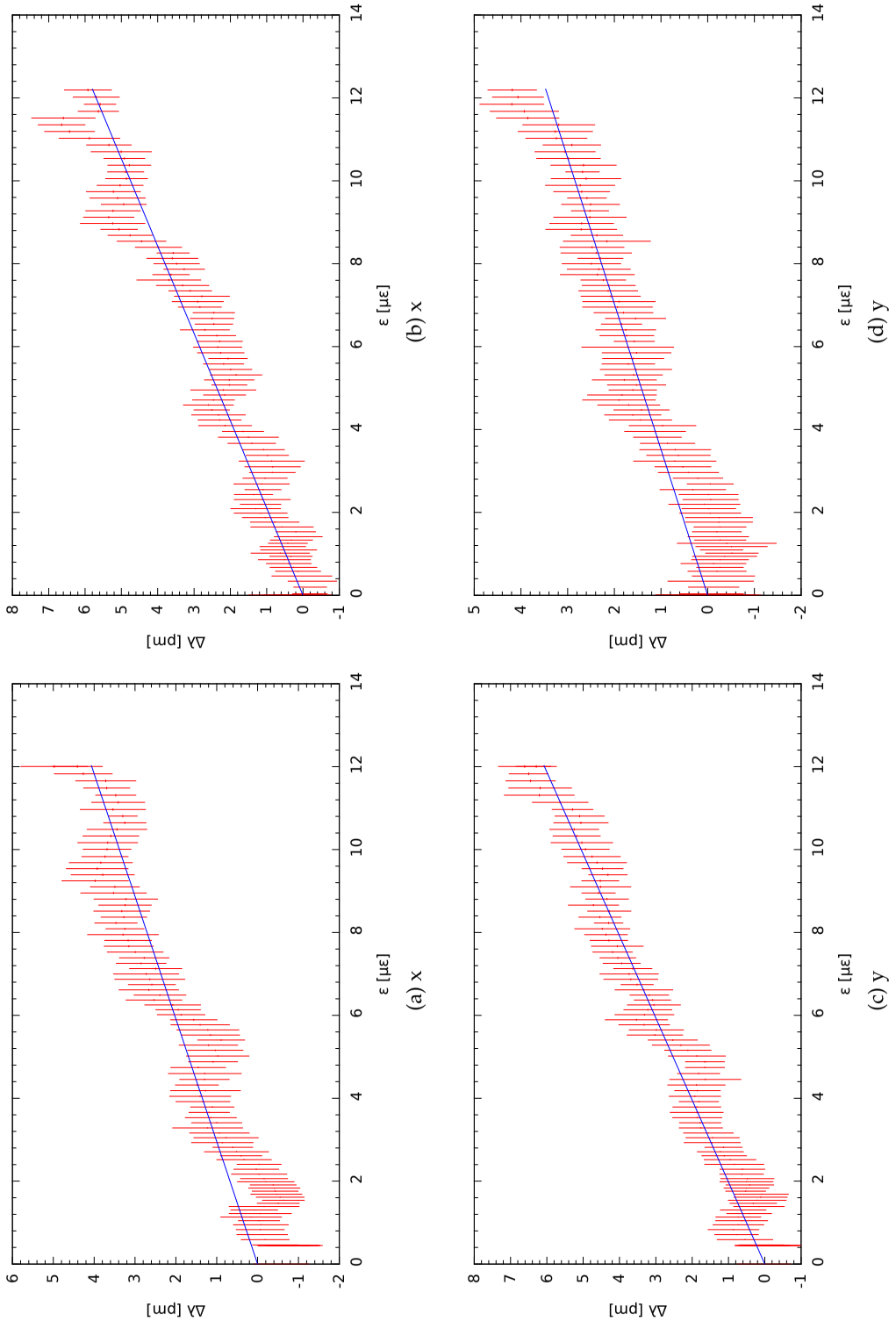

Figure C.2: 0 ÷ 10 [kN]

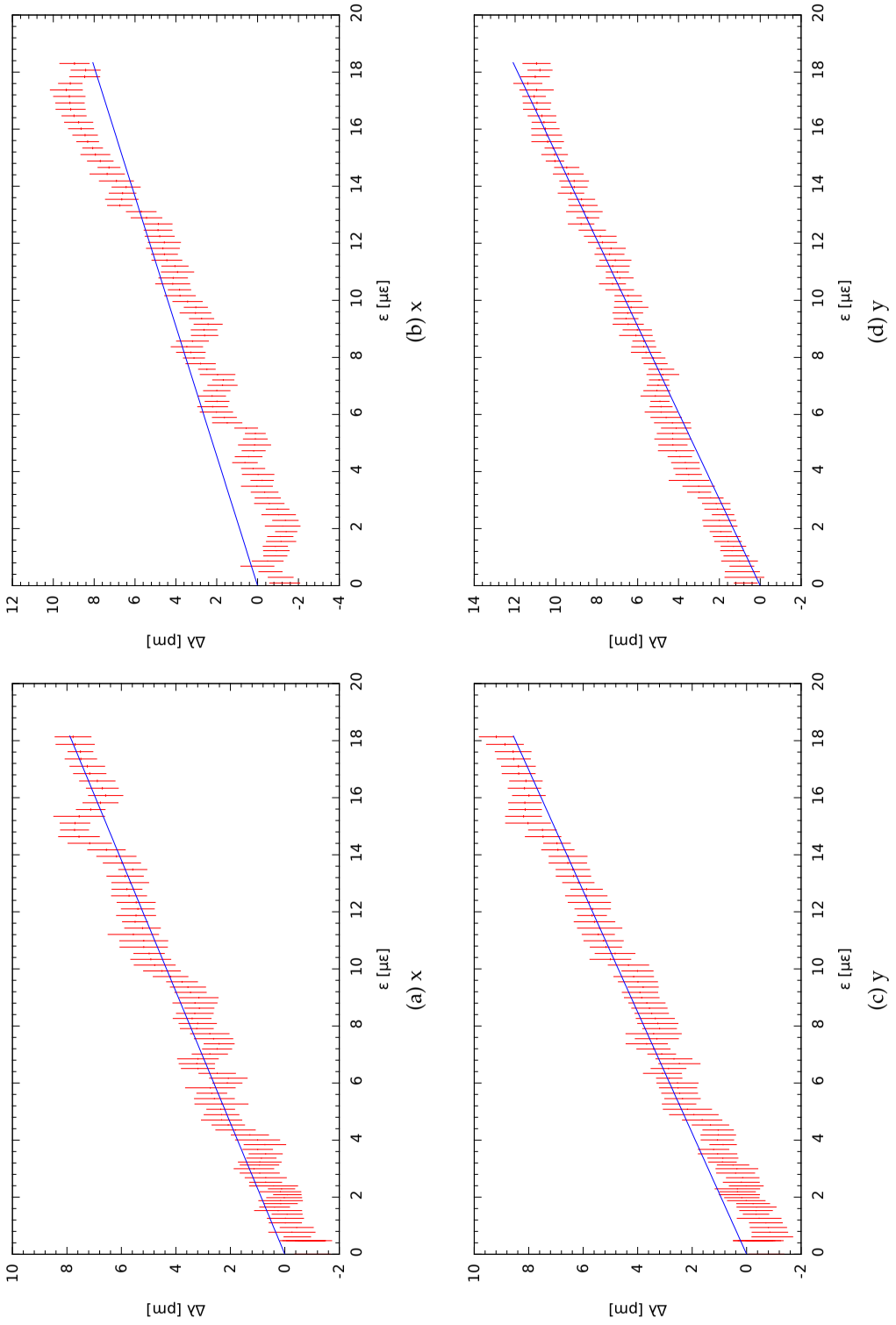

Figure C.3: $0 \div 15$ [kN]

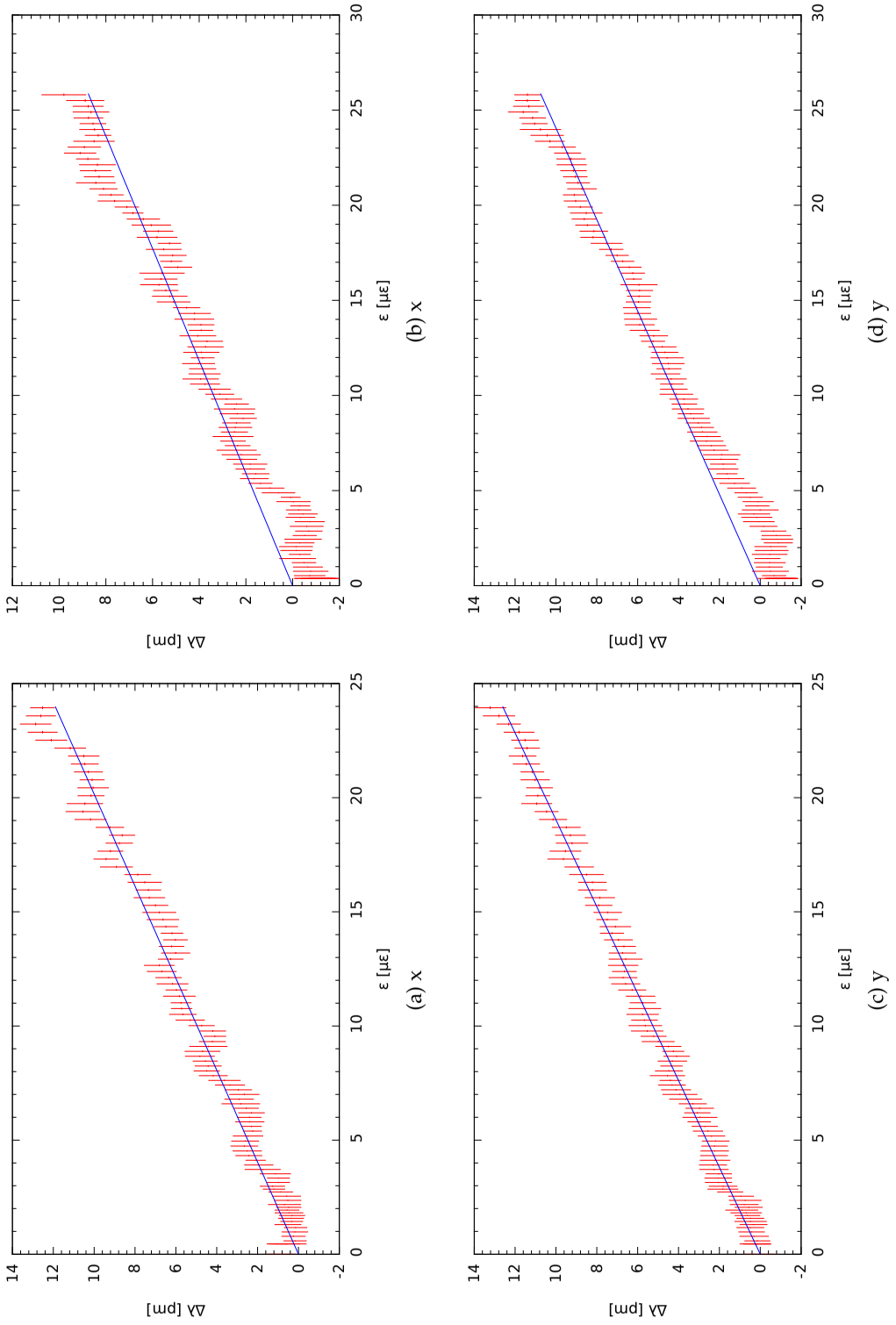

Figure C.4: 0 ÷ 20 [kN]

Bibliography

[1] M. Pregliasco. Tettonica delle placche: Come funziona? — DigiLands, 2013.

[2] N. Facciolini. La preoccupante sequenza sismica nell'Adriatico e la previsione degli effetti delle catastrofi, 2013.

[3] A. Bonaccorso, G. Falzone, and S. Gambino. An investigation into shallow borehole tiltmeters. *Geophys. Res. Lett.*, 26(11):1637–1640, 1999.

[4] G. F. Fernando, A. Hameed, D. Winter, J. Tetlow, J. Leng, R. Barnes, G. Mays, and G. Kister. Structural Integrity Monitoring of Concrete Structures via Optical Fiber Sensors: Sensor Protection Systems. *Struct. Heal. Monit.*, 2(2):123–135, 2003.

[5] Z. Zhou, W. G. Thoms, H. Luke, and J. Ou. Techniques of Advanced FBG sensors: fabrication, demodulation, encapsulation and their application in the structural health monitoring of bridges. *Pacific Sci. Rev.*, 5:116–121, 2003.

[6] Z. Zhou, X. Zhao, W. Li Hong, and J. Ou. Embedded Fbg Strain Sensors and Their Applications in Bridge Health Monitoring.

[7] M. Majumder, T. K. Gangopadhyay, A. K. Chakraborty, K. Dasgupta, and D. K. Bhattacharya. Fibre Bragg gratings in structural health monitoring-Present status and applications. *Sensors Actuators A Phys.*, 147(1):150–164, 2008.

[8] P. Biswas, S. Bandyopadhyay, K. Kesavan, S. Parivallal, B. A. Sundaram, K. Ravisankar, and K. Dasgupta. Investigation on packages of fiber Bragg grating for use as embeddable strain sensor in concrete structure. *Sensors Actuators A Phys.*, 157(1):77–83, 2010.

[9] P. Ferraro and G. De Natale. On the possible use of optical fiber Bragg gratings as strain sensors for geodynamical monitoring. *Opt. Lasers Eng.*, 37(2-3):115–130, 2002.

[10] J. R. Moore, V. Gischig, E. Button, and S. Loew. Rockslide deformation monitoring with fiber optic strain sensors. *Nat. Hazards Earth Syst. Sci.*, 10(2):191–201, 2010.

[11] Z. He, Q. Liu, and T. Tokunaga. Ultrahigh resolution fiber-optic quasi-static strain sensors for geophysical research. *Photonic Sensors*, 3(4):295–303, 2013.

[12] L. D. Landau and E. M. Lifšic. *Teoria dell'elasticità*. Editori Riuniti, 1978.

[13] M. R. Leeder and M. Pérez-Arlucea. *Physical Processes in Earth and Environmental Sciences*. John Wiley & Sons, 2009.

[14] D. Colladon. Sur les réflexions d'un rayon de lumière à l'intérieur d'une veine liquide parabolique. *Comptes Rendus*, 15:800–802, 1842.

[15] J. Babinet. Note sur la transmission de la lumière par des canaux sinueux. *Comptes Rendus*, 15:802, 1842.

[16] R Tricker. *Optoelectronics and Fiber Optic Technology*. Elsevier Science, 2002.

[17] A. Othonos. REVIEW ARTICLE Fiber Bragg gratings. *Rev. Sci. Instrum.*, 68(12):4309–4341, dec 1997.

[18] K. O. Hill, Y. Fujii, D. C. Johnson, and B. S. Kawasaki. Photosensitivity in optical fiber waveguides: Application to reflection filter fabrication. *Appl. Phys. Lett.*, 32(10):647,

1978.

[19] M Bass, J. M. Enoch, E. W. Van Stryland, and W. L. Wolf. *Handbook of Optics, Third Edition Volume IV: Optical Properties of Materials, Nonlinear Optics, Quantum Optics (set): Optical Properties of Materials, Nonlinear Optics, Quantum Optics (set)*. Handbook of Optics. McGraw-Hill Education, 2009.

[20] J. Stone. Photorefractivity in GeO2-doped silica fibers. *J. Appl. Phys.*, 62(11):4371, 1987.

[21] G. Meltz, W. W. Morey, and W. H. Glenn. Formation of Bragg gratings in optical fibers by a transverse holographic method. *Opt. Lett.*, 14(15):823, aug 1989.

[22] R. Kashyap, J.R. Armitage, R. Wyatt, S.T. Davey, and D.L. Williams. All-fibre narrowband reflection gratings at 1500 nm. *Electron. Lett.*, 26(11):730–732, may 1990.

[23] B. J. Eggleton, P. A. Krug, L. Poladian, K. A. Ahmed, and H.-F. F Liu. Experimental demonstration of compression of dispersed optical pulses by reflection from self-chirped optical fiber Bragg gratings. *Opt. Lett.*, 19(12):877, jun 1994.

[24] H. G. Limberger, P. Y. Fonjallaz, P. Lambelet, R. P. Salathe, C. Zimmer, and H. H. Gilgen. OLCR Characterization of Efficient Bragg Gratings in Optical Fiber. In Francois Ouellette, editor, *Opt. Quebec*, pages 272–283. International Society for Optics and Photonics, 1993.

[25] K. O. Hill, B. Malo, F. Bilodeau, D. C. Johnson, and J. Albert. Bragg gratings fabricated in monomode photosensitive optical fiber by UV exposure through a phase mask. *Appl. Phys. Lett.*, 62(10):1035, 1993.

[26] C. Yang and Y. Lai. Apodised fiber Bragg gratings fabricated with a uniform phase mask using Gaussian beam laser. *Opt. Laser Technol.*, 32(5):307–310, jul 2000.

[27] M.C. Gower and S.J. Mihailov. Recording of efficient high-order Bragg reflectors in optical fibres by mask image projection and single pulse exposure with an excimer laser. *Electron. Lett.*, 30(9):707–709, apr 1994.

[28] B. Malo, K. O. Hill, F. Bilodeau, D. C. Johnson, and J. Albert. Point-by-point fabrication of micro-Bragg gratings in photosensitive fibre using single excimer pulse refractive index modification techniques. *Electron. Lett.*, 29(18):1668, 1993.

[29] K. O. Hill and G. Meltz. Fiber Bragg grating technology fundamentals and overview. *J. Light. Technol.*, 15(8):1263–1276, 1997.

[30] D. K. W. Lam and B K Garside. Characterization of single-mode optical fiber filters. *Appl. Opt.*, 20(3):440, feb 1981.

[31] R. Kashyap. *Fiber Bragg Gratings*. Academic Press, San Diego, 1 edition, 1999.

[32] D. C. Johnson, K. O. Hill, F. Bilodeau, and S. Faucher. New design concept for a narrowband wavelength-selective optical tap and combiner. *Electron. Lett.*, 23(13):668, 1987.

[33] C. M. Ragdale, T. J. Reid, D. C. J. Reid, A. C. Carter, and P. J. Williams. Integrated laser and add-drop optical multiplexer for narrowband wavelength division multiplexing. *Electron. Lett.*, 28(8):712, 1992.

[34] L. Reekie, R. Mears, S. Poole, and D. Payne. Tunable single-mode fiber lasers. *J. Light. Technol.*, 4(7):956–960, 1986.

[35] K. O. Hill, B. Malo, K. A. Vineberg, F. Bilodeau, D. C. Johnson, and I. Skinner. Efficient mode conversion in telecommunication fibre using externally written gratings. *Electron. Lett.*, 26(16):1270, 1990.

[36] K. O. Hill, F. Bilodeau, B. Malo, and D. C. Johnson. Birefringent photosensitivity in monomode optical fibre: application to external writing of rocking filters. *Electron. Lett.*, 27(17):1548, 1991.

[37] J.A.R. Williams, N.J. Doran, K. Sugden, and I. Bennion. Fibre dispersion compensation

using a chirped in-fibre Bragg grating. *Electron. Lett.*, 30(12):985–987, jun 1994.

[38] M. M. Werneck, R. C. S. B. Allil, B. A. Ribeiro, and F. V. B. De Nazaré. *Current Trends in Short- and Long-period Fiber Gratings*. InTech, may 2013.

[39] E. Maccioni, N. Beverini, M. Morganti, F. Stefani, R. Falciai, and C. Trono. Low-frequency strain sensor using a fiber Bragg laser. *Nuovo Cim. B*, 122(6-7):751–757, 2007.

[40] S. M. M. Quintero, A. M. B. Braga, H. I. Weber, A. C. Bruno, and J. F. D. F. Araújo. A Magnetostrictive Composite-Fiber Bragg Grating Sensor. *Sensors*, 10(9):8119–8128, aug 2010.

[41] D. R. Lyons, J. V. Lindesay, and C. J. Quiett. Design of Fiber Optic Sensors for Measuring Hydrodynamic Parameters. mar 2001.

[42] N. Beverini, S. Firpi, P. Guerrini, E. Maccioni, A. Mauger, M. Morganti, F. Stefani, and C. Trono. Experimental test of a Fibre Laser Hydrophone Array. In Papadakis J. S. and Bjørnø Leif, editors, *4th Intern. Conf. Exhib. "Underwater Acoust. Meas. Technol. Results"*, pages 829–833, Kos, 2011.

[43] W. Zhou, X. Dong, Y. Jin, and C. Zhao. Cantilever-based FBG sensor for temperature-independent acceleration measurement Wenjun. In Xingde Li, Qingming Luo, Vasilis Ntziachristos, and Yoshiaki Yasuno, editors, *Commun. Photonics Conf. Exhib. (ACP), 2009 Asia*, volume 2009-Suppl, pages 763413–763413–6, nov 2009.

[44] A. Hameed, G. F. Fernando, R. D. Hetherington, J. L. Brown, and R. A. Barnes. Investigation of strain transfer to a sensor protection system embedded in concrete using finite element analysis. *Mater. Struct.*, 35(253):557–563, 2002.

[45] W. C. Zhu, L. Ling, C. A. Tang, Y. M. Kang, and L. M. Xie. The 3D-numerical simulati on on failure process of concrete-filled tubular (CFT) stub columns under uniaxial compression. *Comput. Concr.*, 9(4):257–273, 2012.

[46] L. Ren, J. Chen, H. N. Li, G. Song, and X. Ji. Design and application of a fiber Bragg grating strain sensor with enhanced sensitivity in the small-scale dam model. *Smart Mater. Struct.*, 18(3):035015, 2009.

[47] M. Orazi, R. Peluso, M. Martini, C. Buonocunto, M. Capello, and A. Caputo. L'acquisitore a basso consumo gilda. In *I Work. Tec. Monit. Sism. DEL Territ. Naz.*, pages 86–88, Roma, 2010.

[48] M.K. Smit. New focusing and dispersive planar component based on an optical phased array. *Electron. Lett.*, 24(7):385–386, 1988.

[49] S. Hui and G. H. Xu. A novel fiber Bragg grating interrogating sensor system based on AWG demultiplexing. *Opt. Commun.*, 275(1):196–200, jul 2007.

[50] W. R. Allan, Z. W. Graham, J. R. Zayas, D. P. Roach, and D. A. Horsley. Multiplexed Fiber Bragg Grating Interrogation System Using a Microelectromechanical FabryPerot Tunable Filter. *IEEE Sens. J.*, 9(8):936–943, aug 2009.

[51] J. Cui, Y. Hu, K. Feng, J. Li, and J. Tan. FBG Interrogation Method with High Resolution and Response Speed Based on a Reective-Matched FBG Scheme. *Sensors (Basel).*, 15(7):16516–35, 2015.